UiT The Arctic University of Norway

Faculty of Science and Technology - Department of Physics and Technology

Wind resource assessment using weather research and forecasting model
A case study of the wind resources at Havøygavlen wind farm

Anders Aarhuus Fossem

Master's Thesis in Energy, Climate and Environment …. EOM-3901 …. december 2019

Abstract

The need for energy increases globally due to rapid expansion of population and prosperity. To meet this demand while decreasing carbon emission and eventually transition out fossil fuel, efficient utilization of wind power is prominent. This study evaluates the performance of the Weather Research and Forecast model (WRF) with respect to wind speed and wind direction. The area of the study is the northernmost wind farm site in the world, Havøygavlen. It is located just about 50 kilometers southwest of the North cape, consisting of a complex and coastal terrain. The model simulation period was the entire year of 2017, and the resulting estimates where compared to on-site data measured at hub height at each of the 16 turbines located at the site.

In terms of forecasting capability, the Model was evaluated using correlation, Root Mean Square Error and Bias. The assessment showed little agreement and implementing finer resolution displayed no apparent improvements. The estimate was particularly vulnerable to sudden changes in wind speed, and performed more accurately in periods of low to moderate wind speeds.

Annual weather resource assessment of the site was performed using box plots, annual average wind maps and wind speed histograms. The model is unsuccessful at capturing the high complexity of the terrain, ultimately leading to an underestimation of the wind resources. However, enhanced domain resolution improved the predictive performance, which agreed adequately with the on-site measurements. Furthermore, the annual average wind maps provided valuable knowledge about the local wind patterns surrounding the site.

Annual wind roses and wind fields at specific times of high wind speed occurrence was used to evaluate the model's estimated wind direction. Enhanced domain resolution showed improved directional stability and ability to capture the terrain's effect on the wind before arriving at the site. As a preliminary wind resource tool, the model performs sufficiently, despite the complex terrain of the studied area.

Acknowledgements

First and foremost, I would like to thank my supervisor Yngve Birkelund for your guidance, ideas and useful discussions. I would also like to thank you for proof-reading the thesis, and not least for your full transparency in providing useful scripts for the thesis.

Thanks to Arctic wind for providing on-site measurements, for answering my questions and providing valuable information regarding Havøygavlen.

Many thanks to Kine Solbakken for supplying your script on interpolation between simulation segments.

Last but not least, I would like to thank my family and friends for your support, especially my parents for the continuous encouragement, and for proof-reading this thesis.

Anders Aarhuus Fossem

Tromsø, December 2019

Abbreviations

ECMWF: European Centre for Medium-range Weather Forecasts

ERA: ECMWF reanalysis

ERA-Interim: ECMWF continuously updated global atmospheric reanalysis

NCAR: National Center for Atmospheric Research

MMM: Mesoscale and Microscale Meteorology Division

WRF: Weather research and forecasting model

WPS: WRF pre-processing system

ARW: Advanced Research WRF

NMM: Nonhydrostatic Mesoscale Model

GRIB: GRIdded Binary or General Regularly-distributed Information in Binary form

RK: Runge-Kutta. Numerical integration methods used to solve differential equations. The order of the method is given by an adjoint number, e.g. RK_2 is the 2nd order numerical technique.

CFL: Courant-Fredrichs-Lewy. Condition for stable numerical integration.

FDDA: four-dimensional data assimilation

D01: outermost domain used in this thesis with the highest resolution

D02: Intermediate domain used in this thesis with the highest resolution

D03: Innermost domain used in this thesis with middle resolution

NCL: NCAR command language

TRI: topographic ruggedness index

List of figures

List of tables

Table of Contents

1 Introduction

1.1 The importance of accurate wind prediction

The global energy demand continuous to increase rapidly due to the expansion of prosperity in the world as well as the population in total [1]. The dual challenge of producing a sufficient amount of energy for a growing global demand, while at the same time emitting less carbon, calls for renewable energies to gradually transition into the leading source of power in the future [2]. To supply this demand, all renewable energies must be utilized efficiently by optimizing all part of its production. As one of the leading renewable energies, wind power has accounted for one of the largest shares of overall renewable growth the past years [3], increasing the importance of accurate wind assessments.

The stochastic nature of wind speed and wind direction leads to an intermittent harvest of power compared to the more traditional sources of energy generation, such as fossil fuels. Hence, precise wind resource assessments decreases the need for supplementary balancing energy and integrating energy reserves, thus lowering the production cost of the power generation [4].

1.2 Havøygavlen wind farm

This thesis studies the wind farm site Havøygavlen, located at Havøya in the county of Finnmark in Northern Norway. The wind farm in situated just about 50 kilometers southwest of the North cape in air distance, making it the northernmost wind farm in the world [5]. The turbines are placed on a headland roughly 200 meters above sea level with few towering hilltops surrounding the site, leading to stable wind conditions. However, the coastal landform surrounding the site consist of sheer drops to the ocean, as well as rugged landscapes such as fjords and straits enclosing the site. To capture the complexity of the terrain can therefore be challenging, and may affect the performance of wind prediction [6] [7].

1

The wind park begun its production in October 2002 with 16 operational Nordex N80 windmills with a rated power of 2,5 megawatts and a hub height of 80 meters. In late 2010 one of the original windmills were dismounted and replaced by a SWT-3.0-101 [8], with a rated power of 3,0 megawatts and a hub height of 80 meters. The new turbine consist of fewer moving part and a gearless design with the intention of reducing maintenance operational costs. Hereafter, the wind park has had an installed capacity of 40 megawatts, and an expected energy production of up to 120 Gigawatt hours annually. The wind park is owned and operated by Arctic wind, a subsidiary company of Finnmark Kraft [9].

The geographical placement of each of the 16 windmills in the wind park with accompanying name identification is illustrated in figure 1.1. The turbines are parallelly arranged in two rows, with approximately 300-400-meter gaps between the them. The most recently installed SWT-3.0-101 turbine is called HAV-WTG004, and is situated southeasternmost of the site. Further information regarding specific geographic coordinates of each wind turbine is appended in Appendix A.

Figure 1.1: geographical placement of each windmill at Havøygavlen. The image is obtained from google maps.

1.3 Prior research

The WRF model is a numerical weather prediction and atmospheric simulation system that undergoes comprehensive testing frequently and has shown to give adequate first estimates, and can be used to locate possible new wind farm establishments with promising chances of effective wind power utilization [6] [7].

Prior research comparing on-site measurements to the a WRF model have found that the results from the simulation correlate sufficiently with the observations. Byrkjedal and Berge [7] found that WRF model predicted absolute wind speed accurately at smooth terrain, while at specific heights the surface roughness and topography of sub-grid scale made the model overestimate the wind speed. They also found that the model underestimated the wind at hilltops. A similar study done by Solbakken and Birkelund [6] for a complex and costal terrain in Northern Norway found good agreements for two out of three locations comparing the annual averages of the WRF simulations and the observations. Regardless, the statistical correlations showed similar difficulties with accurate wind speed for complex terrain.

1.4 Purpose of study

The purpose of this study is to run a WRF simulation for the Havøygavlen wind farm site, using suitable parameterizations for the characteristic terrain of the site. The WRF model setup depends on numerous physical and numerical options, making the complex configuration of the model essential to achieve an optimal wind resource assessment for the location at hand [10]. The simulation period will be for the entire year of 2017, to obtain information concerning seasonal behaviour of the wind resources surrounding the site.

The results from the WRF simulation will be compared with on-site measurements using statistical techniques in order to evaluate the performance of the model. The prime interest will be to examine the estimated horizontal wind speed and its prevailing direction at points of interest that correspond to the location where actual on-site measurements has taken place. On the basis of the year-long simulation, specific points in time where estimates consist of particularly high wind will be thoroughly investigated.

3

Additionally, the area surrounding the wind park site will be assessed as a whole using average wind maps displaying the mean wind speed over the entire simulation period. As such, the wind resources of the site, as well as the impact of surrounding terrain can be evaluated.

An adequate wind research assessment for the Havøygavlen site can be used as valuable information for a further expansion of the site, on the grounds that the on-site measurements provides information on weather and wind from a specific point, while the WRF simulation maps the entire surroundings of the site. WRF modelling in the complex terrain at Havøygavlen can contribute with valuable knowledge and insight regarding wind resources, which can be transferred to sites of similar terrain.

2 Theory

2.1 Fluid dynamics

Governing equations of fluid dynamics are fundamental for a theoretically analysis of air motion. These equations of fluid motion involve partial differential equation systems derived from physical principles such as conservation of mass, momentum and energy [11]. Some assumptions and simplification must be done when deriving these equations. The fluid is studied at a macroscopic level, and it can therefore be treated as a continuous medium. The fluid is also assumed to be incompressible. There are two different methods of describing the flow of a fluid. The Eulerian description considers the fluid flow by focusing on a specific fluid element with a fixed space which the fluid flows through, as time passes. The Lagrangian method describes the flow as being comprised of fluid particles with a finite size. The following derivations of conservation of mass and momentum follows the derivation presented in [11], while the energy conservation derivation follows the derivation used in [12].

2.1.1 Conservation of mass

Considering a fixed mass m of fluid enclosed in a region $R(t)$ in space. The mass is then given by:

$$m = \int_{R(t)} \rho dV \tag{2.1}$$

Where p is the pressure and dV is the volume element. The mass is thought to be conserved, and the rate of change of mass in the region $R(t)$ as time passes is zero:

$$\frac{dm}{dt} = 0 \tag{2.2}$$

By combining eqs. (2.1) and (2.2) we obtain:

$$\frac{dm}{dt} = \frac{d}{dt}\int_{R(t)} \rho dV = 0 \tag{2.3}$$

By applying the general transport theorem to eq. (2.3), and locally defining *R(t)* as an arbitrary fluid element, it can be expressed as:

$$\int_{R(t)} \frac{\partial \rho}{\partial t} dV + \int_{S(t)} pU \cdot ndA = 0, \tag{2.4}$$

where *U* is the flow velocity, and *n* is the outward-pointing unit normal vector, *S(t)* is the boundary of *R(t)*, and *dA* is the surface element.

At this point the equation contains two separate integrals over the volume and surface of the fluid element, respectively. The surface integral can be converted into a volume integral by applying the Gauss's theorem:

$$\int_{S(t)} pU \cdot ndA = \int_{R(t)} \nabla \cdot \rho U \, dV \tag{2.5}$$

Eq. (2.5) can now be substituted into eq. (2.4) and we obtain the following:

$$\int_{R(t)} \frac{\partial \rho}{\partial t} dV + \nabla \cdot \rho U \, dV = 0 \tag{2.6}$$

The region *R(t)* is defined to be arbitrary and can consequently be formed arbitrarily small within the borders of the criteria for assuming a continuous fluid. This implies that within the region *R(t)* the integrand must be equal to zero. Eq. (2.6) can therefore be written as follows:

$$\frac{\partial \rho}{\partial t} + \nabla \cdot \rho U = 0, \tag{2.7}$$

and in Cartesian coordinates where x = (x, y, z), U = (u, v, w):

$$\frac{\partial \rho}{\partial t} + \frac{\partial \rho u}{\partial x} + \frac{\partial \rho v}{\partial y} + \frac{\partial \rho w}{\partial z} = 0 \tag{2.8}$$

For incompressible fluids $\frac{\partial \rho}{\partial t} = 0$ eq. (2.8) can be rewritten as:

$$\frac{\partial u}{\partial x} + \frac{\partial v}{\partial y} + \frac{\partial w}{\partial z} = 0 \qquad (2.9)$$

The given equation is often referred to as the continuity equation and explains how the fluid conserves mass in its motion.

2.1.2 Conservation of momentum

Unlike the derivation of the differential equation describing conservation of mass, we will in this case from the start define a region *R(t)* restricted to be a fluid element. We want to employ Newton's second law in a general form that expresses the time rate of change of momentum of a material region being equal to the sum of the forces that act on the material region [11]:

$$\left\{ \begin{matrix} sum\ of\ forces\ acting \\ on\ the\ material\ region \end{matrix} \right\} = \left\{ \begin{matrix} time\ rate\ of\ change\ of \\ momentum\ of\ a\ material\ region \end{matrix} \right\} \qquad (2.10)$$

By recalling that the momentum is given by mass times velocity *mu,* we can express the force *F* by Newton's second law as follows:

$$F = \frac{d(mu)}{dt} \qquad (2.11)$$

For convenience later in the derivations we want eq. (2.10) to be expressed by the same variables as conservation of mass equation in cartesian coordinates. This can be done by solving for the force per unit volume *V* acting on the material region:

$$\frac{F}{V} = \frac{d(pu)}{dt} \qquad (2.12)$$

We advance with an Eulerian view for the flow of the fluid, and acknowledge that the time-rate of change of momentum should be represented by the material derivative. For the complete velocity vector *U*, we obtain:

$$\frac{d}{dt} \int_{R(t)} \rho U\ dV \equiv \{time\ rate\ of\ change\ of\ momentum\ vector\} \qquad (2.13)$$

7

The forces that account for the sum of forces acting on the material region are the body forces F_b acting on the fluid element $R(t)$, and the surface forces F_b which only act on the surface $S(t)$ of $R(t)$. We substitute this for the sum of forces in eq. (2.10) and obtain:

$$\frac{d}{dt} \int_{R(t)} \rho U \, dV = \int_{R(t)} F_b \, dV + \int_{S(t)} F_s \, dA \qquad (2.14)$$

As was done for the conservation of mass derivation, we want to manipulate the equation such that the result consists of only volume integrals. By applying Reynolds transport theorem [11] to eq. (2.14) we obtain:

$$\frac{d}{dt} \int_{R(t)} \rho u \, dV = \int_{R(t)} \frac{\partial \rho u}{\partial t} \, dV + \int_{S(t)} \rho u U \cdot n \, dA \qquad (2.15)$$

Applying Gauss's theorem on the surface integral gives the following result:

$$\int_{R(t)} \frac{\partial \rho u}{\partial t} + \nabla \cdot (\rho u U) \, dV \qquad (2.16)$$

This correspond to the right hand side of eq. (2.15). The second term of the equation, $\nabla \cdot (\rho u U)$, can be simplified by using the product-rule differentiation and implementing the condition of incompressible flow stating that $\nabla \cdot U = 0$ and that the pressure is constant:

$$\nabla \cdot (\rho u U) = \rho U \cdot \nabla u \qquad (2.17)$$

By substituting the result from eqs. (2.16) and (2.17) into eq. (2.15) we get the following:

$$\frac{d}{dt} \int_{R(t)} \rho u \, dV = \int_{R(t)} \frac{d \rho u}{dt} \, dV \qquad (2.18)$$

We implement eq. (2.18) into eq. (2.14):

$$\int_{R(t)} \frac{d \rho U}{dt} \, dV = \int_{R(t)} F_b \, dV + \int_{S(t)} F_s \, dA \qquad (2.19)$$

The most common force associated with body forces is a buoyancy force F_b as a result of gravitational acceleration g. Commonly this force is given by $F_b = pg$. When it comes to the surface force F_s, since F_b and ρU are vector, so must apply for the surface force as well.

8

This implies that there must exist a matrix, let's call it τ, such that $F_s = \tau \cdot n$, where n is the outward unit normal vector to the surface $S(t)$. Then eq. (2.19) can be rewritten as:

$$\int_{R(t)} \frac{d\rho U}{dt}\, dV = \int_{R(t)} pg\, dV + \int_{S(t)} \tau \cdot n\, dA \qquad (2.20)$$

Once again, we apply Gauss's theorem to the surface integral, and rearrange the equation. Additionally, we remember that the arbitrary fluid can be selected to be arbitrary small, and consequently it follows that within the region $R(t)$ the integrand must be equal to zero. Ultimately, we obtain the following result:

$$\frac{d\rho U}{dt} - pg - \nabla \cdot \tau = 0 \qquad (2.21)$$

This equation gives a general illustration of the conservation of momentum for all points of any fluid flow.

2.1.3 Conservation of energy

The first law of thermodynamics states that energy must be conserved. For an ideal fluid flowing steadily through a control volume as displayed in figure 2.1 the Bernoulli's equation can be derived to prove the conservation of energy principle [12].
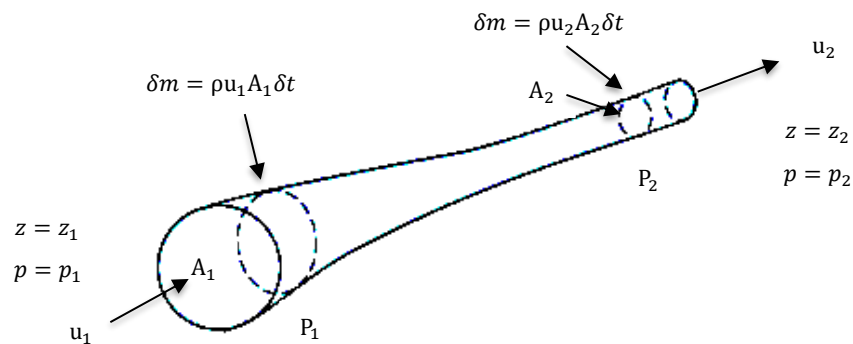
Figure 2.1: Control volume for Bernoulli's equation. The figure is retrieved from *[12]*.

At any point p_i of the control volume, the velocity, pressure, height and cross-sectional area are denoted by u_i, p_i, z_i, and A_i, respectively. The change in gravitational potential energy of the mass δm from height z_1 to z_2 is given by $\delta m g(z_2 - z_1)$, and the change in kinetic energy from velocity u_1 to u_2 is given by $\frac{1}{2}\delta m(u_2 - u_1)^2$.

The mass of fluid that enters the control volume in the time interval δt at point P_1, and the mass of fluid leaving point P_2, respectively, is given by:

$$\delta m = \rho u_1 A_1 \delta t \ , \qquad \delta m = \rho u_2 A_2 \delta t \tag{2.22}$$

The fluid can only enter the control volume by overcoming the pressure p_1 done by the fluid. For a small distance $\delta s_1 = u_1 \delta t$ the applied work that pushes the mass δm at point P_1, and the work done pushing the mass δm out of the control volume at point P_2, respectively, is given by:

$$\delta W_1 = p_1 A_1 \delta s_1 = p_1 A_1 u_1 \delta t \ , \quad \delta W_2 = -p_2 A_2 \delta s_2 = -p_2 A_2 u_2 \delta t \tag{2.23}$$

Hence, the net work done is given by:

$$\delta W_1 + \delta W_1 = p_1 A_1 u_1 \delta t - p_2 A_2 u_2 \delta t \tag{2.24}$$

The net work should be equal to the sum of change in potential and kinetic energy, by the principle of energy conservation. We obtain:

$$p_1 A_1 u_1 \delta t - p_2 A_2 u_2 \delta t = \delta m g(z_2 - z_1) + \frac{1}{2}\delta m(u_2 - u_1)^2 \tag{2.25}$$

We substitute the derivations in eq. (2.23) into eq. (2.24) and simplify the result:

$$\frac{p_1}{\rho} + g z_1 + \frac{1}{2}u_2^2 = \frac{p_2}{\rho} + g z_2 + \frac{1}{2}u_1^2 \tag{2.26}$$

Finally, we implement the fact that P_1 and P_2 are arbitrary, and obtain the following result:

$$\frac{p}{\rho} + gz + \frac{1}{2}u^2 = const.$$ (2.27)

at all points along the stream-tubed control volume.

2.1.4 Equation of state

Equation of state refers to the dependency between state variables, such that calculations of a state variable is permitted by the specification of the other state variables. In fluid dynamics the relationship between pressure, temperature, and density is central, and holds for gases with temperatures around moderate to high and pressure around low to moderate. For these criteria the ideal gas law is often employed to relate these properties [11], and can be expressed by the following formula:

$$p = \rho RT \quad or \quad p\alpha = RT$$ (2.28)

Where R is the ideal gas constant given by $R = kn$, where k and n are the Boltzmann's constant and the volume number density of the gas, respectively. T is the absolute temperature, ρ is the density of the fluid, and α is the specific volume of the gas.

2.2 Fundamental Equations of wind power

Wind power is the quantification of the extraction rate of kinetic energy of air in motion [13]. Kinetic energy is given by the following formula:

$$KE = \frac{1}{2}m \cdot U^2$$ (2.29)

Where U and m are the velocity and mass of the moving air, respectively.

11

Volume flow rate is the volume of the flow through an area of interest per unit time and per unit area, $A \cdot U$. The mass flow rate is given by the density of the flow ρ multiplied by the *volume flow rate*:

$$\frac{dm}{dt} = \rho \cdot A \cdot U \qquad (2.30)$$

Wind power quantifies the amount of kinetic energy flowing through a specific area A per unit time:

$$P_W = \frac{1}{2} \dot{m} \cdot U^2 = \frac{1}{2} \frac{dm}{dt} \cdot U^2 \qquad (2.31)$$

We implement eq. (2.30) into eq. (2.31) and obtain:

$$P_W = \frac{1}{2} \frac{dm}{dt} \cdot U^2 = \frac{1}{2} \rho \cdot A \cdot U^3 \qquad (2.32)$$

A wind turbine's power extraction is not ideal, and some of the kinetic energy flowing through will always be lost. The wind turbine's extraction efficiency is given by the ratio of the turbine's utilized power P_T to the total power from the wind P_W, and is called the power coefficient C_P:

$$C_P = \frac{P_T}{P_W} \qquad (2.33)$$

By implementing eq. (2.33) into eq. (2.32) we can express the turbine's power output P_T as follows:

$$P_T = \frac{1}{2} \rho \cdot A \cdot U^3 \cdot C_P \qquad (2.34)$$

Which will always be smaller than P_W since the total energy extraction from air parcels would result in zero momentum and consequently zero downstream velocity, which would block the air flow.

2.3 Betz' limit

Betz' limit is the theoretical upper limit efficiency of a wind turbine, and is derived from the mass, momentum and energy conservation principles [12]. The estimation is done by modelling the turbine as an actuator disc, which is an idealized and infinitely thin disc that induce an air flow with constant velocity along the rotation axis. Such a model is sketched in figure 2.1 which displays the flow upstream and downstream as a stream-tube.
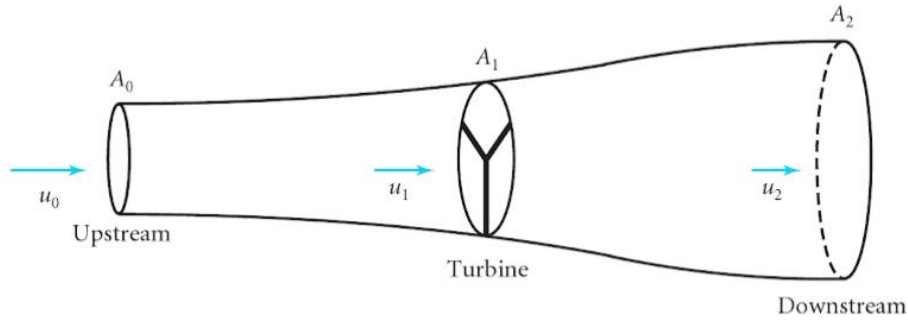
Figure 2.2: Air flow through an idealized wind turbine. The figure is borrowed from *[12]*.

The turbines extraction of kinetic energy from the air flow decreases its speed, which consequently increases the cross-sectional area of the stream-tube due to energy conservation. The thrust force applied on the turbine by the air flow correspond to the rate of change in momentum, which is given by:

$$F_{Thrust} = \frac{dm}{dt}(u_0 - u_2) \tag{2.35}$$

Where $\frac{dm}{dt}$ is the mass flow rate, and the parenthesised term constitute the change in velocity from cross-sectional area A_0 to A_2. The extracted power done by the turbine is given by the thrust F_{Thrust} multiplied by the velocity at the turbine u_1:

$$P = F_{Thrust} \cdot u_1 = \frac{dm}{dt}(u_0 - u_2)u_1 \tag{2.36}$$

Eq. (2.31) expresses the turbine's extracted power by the rate of kinetic energy loss. By comparing the equation with eq. (2.36) we obtain:

$$\frac{dm}{dt}(u_0 - u_2)u_1 = \frac{1}{2}\frac{dm}{dt}\cdot(u_0 - u_2)^2 \tag{2.37}$$

By solving for the wind velocity through the turbine u_1 and the wind speed at the downstream cross-section u_2, respectively, we obtain the following expressions:

$$u_1 = \frac{1}{2}(u_0 + u_2) \quad , \quad u_2 = 2u_1 - u_0 \tag{2.38}$$

We substitute the mass flow rate definition from eq. (2.30), and the derived expression for u_2 from eq. (2.38) into eq. (2.36) and obtain:

$$P = 2\rho u_1 A_1(u_0 - u_1) \tag{2.39}$$

We define an axial induction factor a so that:

$$a \equiv \frac{u_0 - u_1}{u_0} \rightarrow u_1 = (1 - a)u_0 \tag{2.40}$$

We implement the derived expression for u_2 from eq. (2.40) into eq. (2.39) and get:

$$P = 2\rho(1 - a)u_0 A_1(u_0 - (1 - a)u_0) = \frac{1}{2}\rho u_0^3 A_1[4a(1 - a)^2] \tag{2.41}$$

By comparing eq. (2.41) to eq. (2.34) we identify that the square bracketed term constitutes the power coefficient C_P. The maximum value of the power coefficient C_P is found by setting $\frac{dC_p}{dt}$ to zero and solving for the induction factor a:

$$\frac{dC_p}{dt} = \frac{d}{dt}(4a(1 - a)^2) = 0 \rightarrow 12a^2 - 16a + 4 = 0 \tag{2.42}$$

Eq. (2.42) can be solved by using the quadric formula which gives the following result:

$$a = \begin{cases} 1 \\ \frac{1}{3} \end{cases} \tag{2.43}$$

Using induction factor value, $a = 1$, would lead to zero power output. Thus, the maximum value of the power coefficient C_P is therefore found by using the induction factor value $a = \frac{1}{3}$. We substitute this into eq. (2.41) to obtain maximum power P_{max}:

$$P_{max} = \rho u_0^3 A_1 \left[4\frac{1}{3}\left(1 - \frac{1}{3}\right)^2 \right] = \rho u_0^3 A_1 \left[\frac{16}{27}\right] \qquad (2.44)$$

Hence, the upper limit power ratio that can be utilized by the turbine is 16/27 or ~59 %. In reality Betz' limit is unreachable, and most turbines has efficiency values in the 35-45% range [14].

2.4 Power curve

A wind turbine's power curve is a visual representation of the electrical power output generated at a given wind speed. The power curve is based on measurements in low turbulence and with a direct attack angle on the turbine and is a theoretical derivation. In addition, the wind will always fluctuate and hit the turbines at varying directions, hence such a curve only serves as an indication of the possible power output for different wind speeds, while in reality, data points would swarm around the curve [15].

Figure 2.3 (a) shows the power curve for all 15 N80/2500 kW turbines installed at Havøygavlen. Figure 2.3 (b) shows the power curve for the single SWT-3.0-101/3000 kW turbine installed at Havøygavlen. Figure 2.3 (c) shows the combined power curve for entire wind park, in which a uniform wind direction distribution is applied [16]. The turbine does not start producing power until reaching a threshold called the cut-in speed. This is a result of the wind having to generate sufficient torque for the blades of the turbine to start rotating. The most common cut-in speeds for modern turbines are 3-4 m/s.

As the wind speed increases, the power output rapidly rises until reaching a point where the power generation flattens out. At this point the turbine has reach its generation limit, called the rated power output. Usually around the wind speeds of 25 m/s a new threshold exist, called the cut-out speed. This is where the blades of the turbine risks being damage due to the increasing force applied to them, and the turbine is brought to a standstill.
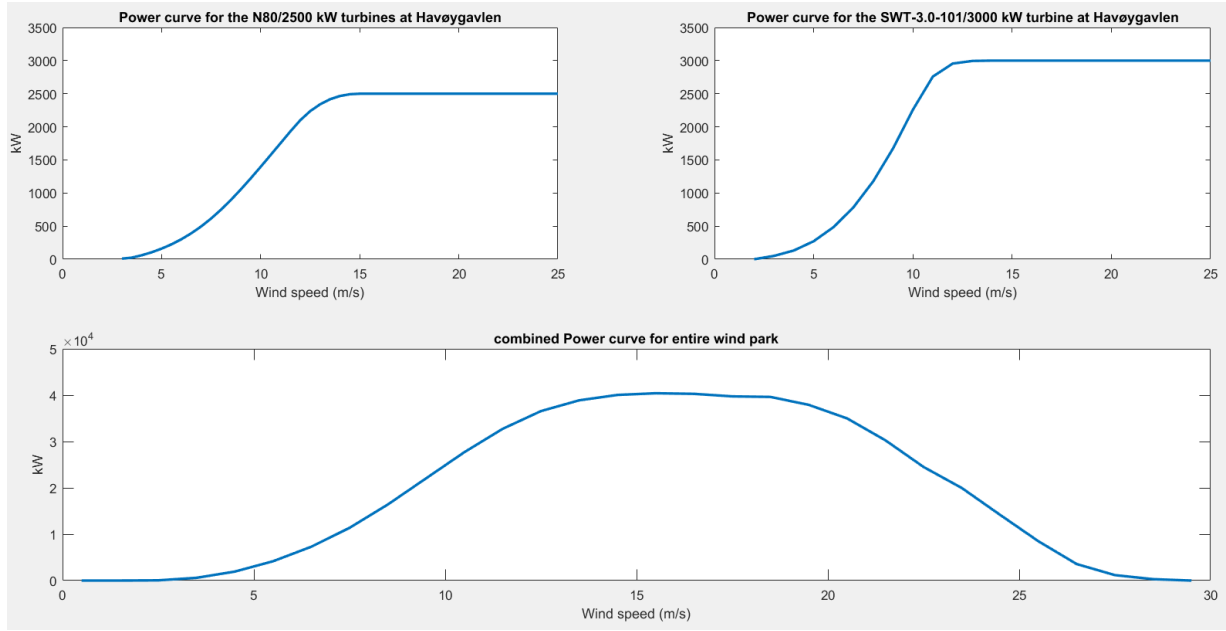
Figure 2.3: (a) Power curve for all 15 N80/2500 kW turbines installed at Havøygavlen. (b) Power curve for the single SWT-3.0-101/3000 kW turbine installed at Havøygavlen. (c) Combined power curve for entire wind park. Data for (a) and (b) was collected from *[17]*, while data for (c) was collected from *[16]*.

2.5 Wind speed extrapolation

By extrapolating the wind speed in relation to height, a vertical wind profile can be formed. An empirical approach to describe this relation often chosen for its mathematical simplicity, is the power law. The law is derived as follows [18]:

$$u(z) = u(z_r) \left(\frac{z}{z_r}\right)^a, \qquad (2.455)$$

where u is the horizontal wind speed, z is the height, z_r is the reference height, and a is the Hellman exponent which depend on surface roughness and stability of the atmosphere. The law imply an exponential relationship between wind speed and altitude, meaning the wind at hub height of 80 meter will have higher speed than closer to the surface.

3 Methodology

3.1 Sources of data

3.1.1 On-site measurements

On site measurements used in this thesis include wind speed and wind direction measured at hub height for each of the 16 wind turbines situated at Havøygavlen. Each measurement was collected by averaging every ten-minute time period to coincide with the history output file interval of the WRF-model. All comparison of on-site measurement regarding wind direction will be collected from the Siemens SWT-3.0-101. This is due to a lack of trustworthy wind direction measurements done by the Nordex wind turbines at the site, as a result of measurements drifting from its directional reference point.

Due to effects of weather factors such as icing or system failures, the rotor blades of the turbines at Havøygavlen may be brought to a standstill for inspection and maintenance. Moreover, fluctuation in wind speed beyond the thresholds of cut-in speed and cut-out speed will also cause a standstill. As a result, the production will not be continuous over the span of a whole year. Figure 3.1 shows the operational state of each turbine installed at Havøygavlen for the whole year of 2017. Plotted lines indicate a running production, while section where the plotted lines are missing indicates all other operational states leading to a production halt.
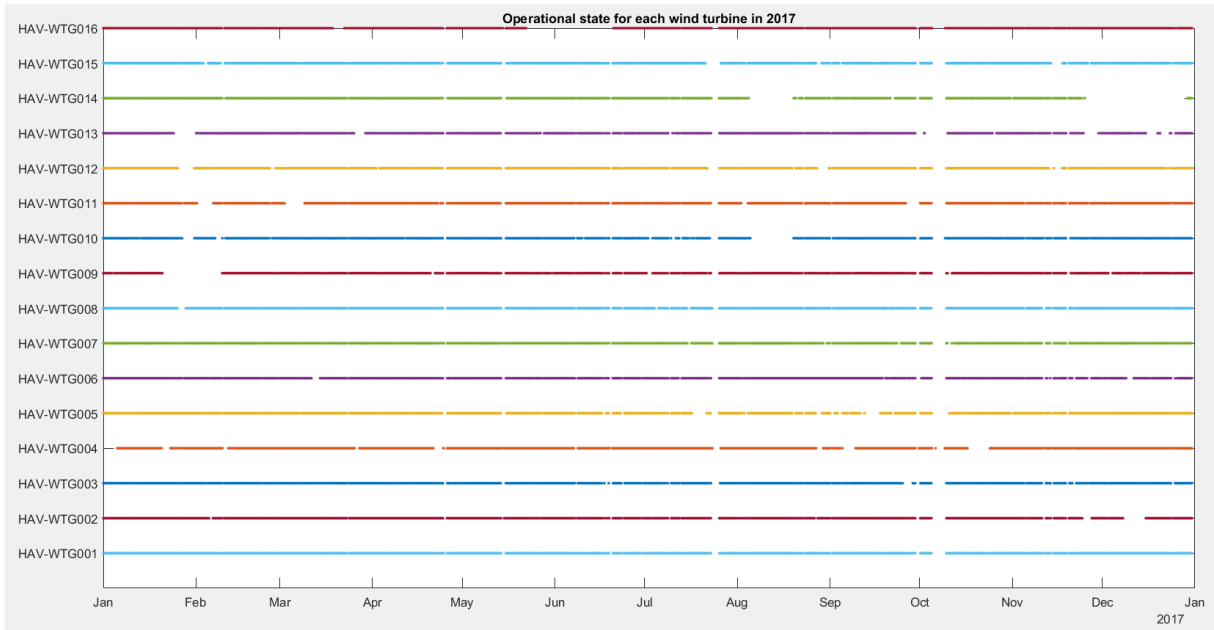
Figure 3.1: operational state of each turbine installed at Havøygavlen in 2017.

3.1.2 ERA-Interim

ERA-Interim is a global reanalysis of the atmosphere covering the time period from 1979 and onwards, extending to near-real time [19], [20]. The data, supplied by the European Centre for Medium-Range Weather Forecasts (ECMWF), depends on prior and real time observational data collected from instruments such as weather station and satellites. The reanalysed data is then produced by a four-dimensional variational assimilation scheme that estimates the global atmosphere's state of progression and underlying surface depending on segments of previous forecasts [21]. ERA-Interim's integrated forecast system has a spatial resolution of approximately 80 kilometers horizontally, and 60 levels in the vertical, of which the top level is situated at 0,1 hPa, which corresponds to approximately 44 kilometers. The ERA-Interim data assimilation provides estimates of the status of the atmosphere four time a day, distributed at 00, 06, 12 and 18 UTC.

3.2 WRF model

The Weather Research and Forecasting (WRF) model is a mesoscale numerical weather prediction system constructed for atmospheric research and operational forecasting applications. The model makes it possible for researchers to create simulations based on idealized and real atmospheric conditions. Its development started in the late 1990's, and in November 2000 it had its first release [22].

The process of development has been a multi-agency effort with central participants such as the National Center for Atmospheric Research's (NCAR) Mesoscale and Microscale Meteorology (MMM) Division, the Center for Analysis and Prediction of Storms (CAPS) at the University of Oklahoma, the National Oceanic and Atmospheric Administration's (NOAA) National Centers for Environmental Prediction (NCEP) and Earth System Research Laboratory (ESRL), and the Department of Defence's Air Force Weather Agency (AFWA) and Naval Research Laboratory (NRL) [10].

The WRF Software Framework (WSF) consists of two dynamics solvers; the Advanced Research WRF (ARW) solver mainly developed by NCAR, and the NMM (Nonhydrostatic Mesoscale Model) solver, which is developed at NCEP. The WRF model's availability as a community model facilitates the possibility for a wide range of contributors to modify and improve aspects of the model such as dynamics, numerics, and physical options. The WRF modelling system flowchart is sketched in figure 3.2, which visualizes one simulation of the model.
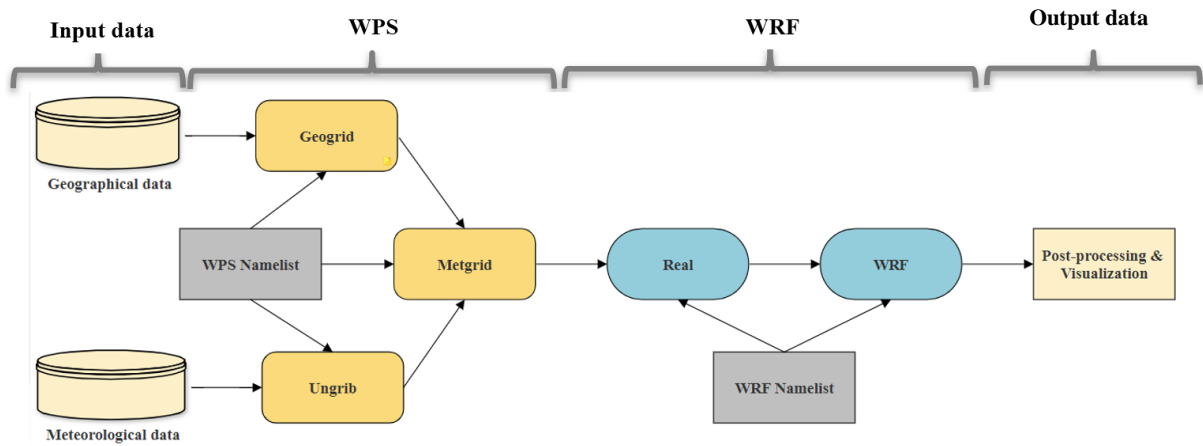
Figure 3.2: WRF modelling system flowchart. Based on description from *[10]*.

3.2.1 WPS

The WRF pre-processing system (WPS) defines the simulation domains, interpolates both terrestrial data and meteorological data into simulation domain, and establishes the boundary and initial values for the simulation. All of these processes are encapsulated in the programs Geogrid, Ungrib and Metgrid, whose role collectively is to arrange and decode input data in such a fashion that it can be fed to the ARW for a real data simulation.

WPS namelist

Each WPS program needs to read of parameters that resides in a common file, called a namelist, as shown in figure 3.2. The first step for the WPS namelist is deciding which dynamics solver to be used in the simulation: ARW or NMM. The WPS programs also read parameters from the WPS namelist that decide the number of domains, start and end time of the simulation, latitude and longitude etc. The namelist file consist of separate and shared records depending on whether parameters are used by one or more of the WPS programs. The namelist for the pre-processing run used in this thesis is appended in Appendix B.

Geogrid

The Geogrid program's task is defining the simulation domains and given all computational grids execute a terrestrial data interpolation. The program provides values for static fields at each model grid point, which is gathered from the WPS namefile. It then creates a landscape model in the simulation domain. This static landscape model is comprised of latitude and longitude computation, map projection, Coriolis parameters at each grid point, vegetation, surface albedo, soil type etc. [23].

Ungrib

The purpose of the Ungrib program is to read and decode gridded binary data files (GRIB) containing time-varying meteorological fields. As shown in figure 3.2 the data file is extracted from the input data process "meteorological data", and is "unpacked" and written in a simpler format called the intermediate format. The GRIB files are often gathered from other global or regional models, and therefore typically contain more fields than are necessary to run the WRF model. To know which field to extract the program uses Vtables (Variable tables) to identify levels and variables within the GRIB file.

Metgrid

As shown in figure 3.2 the output from the Geogrid and Ungrib program is fed to the Metgrid program. The meteorological data extracted from Ungrib is horizontally interpolated to the simulation domains which are defined in the Geogrid program. The Metgrid program rotates the extracted wind data with respect to the WRF grid by paralleling U-components to the x-axis, and paralleling the V-components to the y-axis. Due to the extraction of time-dependent output data from the Ungrib program, Metgrid is also dependent of time.

3.2.2 WRF

WRF namelist

Much like the WPS namelist the WRF program also needs to read of parameters that resides in a file configurating its runtime. The simulation options for WRF collected from the namelist also contains simulation time and domain specifications. However, WRF also require more complex configuration consisting of all necessary dynamic options, physical options, and boundary conditions. Dimensions domains, nesting options, and dates must match those set in the WPS namelist. The namelist for the WRF run used in this thesis is appended in Appendix B.

Real

The "Real" program refers to the use of real data for the WRF simulation. Within the program, both boundary and initial conditions are created. The meteorological fields are extracted from the WPS and vertically interpolated to model levels, and hydrostatic equilibrium is implemented [24]. The output from the Real program is the simulation domain, which is 4-dimensional due to its dependence of space and time.

The ARW also supports the use of an "Ideal" program referring to a WRF simulation with settings for an idealized case with constructed dynamic balance and initial conditions. The output of the real program is input for the run of the actual WRF simulation, and all previous steps are the foundation that the model run depends on.

Domain and nesting options

In this thesis three nested domains with 1:5 ratio between the domain horizontal resolution were chosen. For simplicity, the largest and coarsest domain will hereafter be referred to as D01, the mid-domain will be referred to as D02, and the innermost domain will be referred to as D03. The resolution of D01, D02 and D03 are 25, 5, and 1 kilometers, respectively. Figure 3.3(a) shows the domain configuration setup used in this thesis.

As shown in the figure, all domains are virtually centred to the coordinates of the Havøygavlen wind farm site marked with a white dot, a configuration commonly referred to as telescoping domains. However, the innermost domain is slightly skewed from center to try and capture essential topographic elements surrounding the site, and prevent the lateral boundaries from cutting hilltops or other land shapes affecting the wind, to improve model performance. Figure 3.3(b) illustrate the topography surrounding Havøygavlen within the boundaries of D03, along with a red dot indicating the location of the wind park. Nesting allows for a region of the coarse domain to be focused by applying an additional domain with a finer resolution grid. The grid cells of the nested domain overlap the coarse domain cells at the corresponding cell boundaries. The aim is to remove the need for generalized and complex remapping calculations, and to enhance model flexibility and performance [25]. By applying three nested domains, this process in undergone twice allowing further performance enhancement.

The dynamic solver ARW chosen in all simulations in this thesis, allows the use of both one-way nesting and two-way nesting. One-way nesting refers to how the coarse domain and the nested domain interacting only one way [10]. The solution of the nested domain grid replaces the coarse domain grid at the coincident grid points, but does not distribute back any feedback to the coarse domain. Using one-way nesting is a suitable option for analysing the performance of both the coarse and nested domain, as the coarse domain is not smoothened by the nested domain. In this thesis the one-way nesting is chosen between all three domains due to the primary interest being the examination of the highest resolution domain, D03. However, the coarser domains will also be assessed and treated as a reference point in regard to the D03 performance. ARW also have the option of using 2-way nesting, which in addition to replacing the coarse domain grid with a nested domain, feed information in return to the coarse domain. This way the coarse domain can be smoothened in the area where the nested domain is situated.
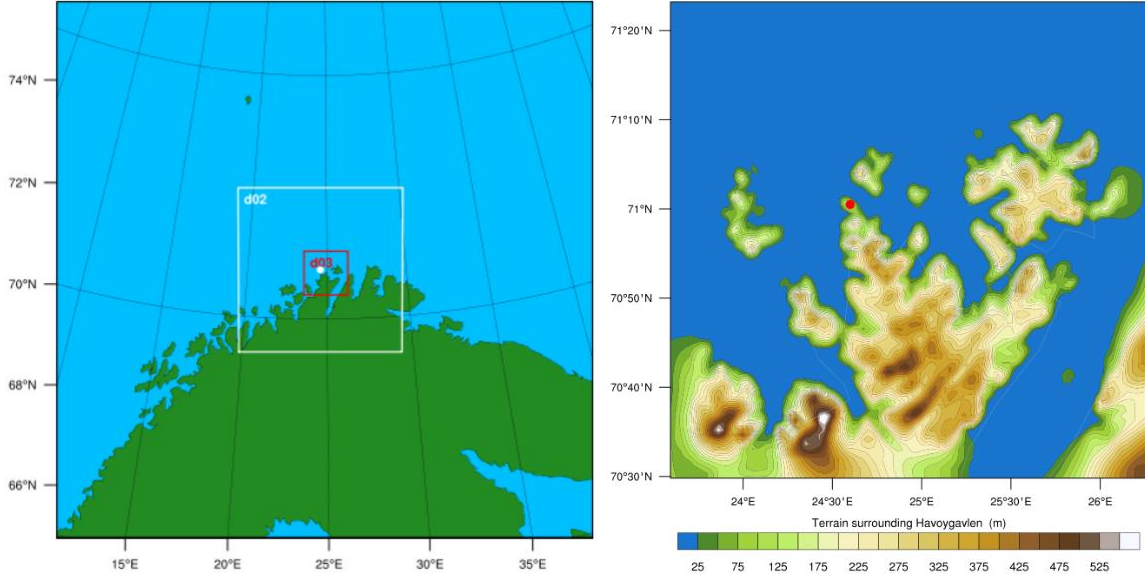
Figure 3.3: (a) Domain configuration setup centred to Havøygavlen. (b) Topography surrounding Havøygavlen confined by D03.

3.2.3 Vertical coordinates

The ARW dynamic solver uses hydrostatic-pressure vertical coordinates denoted by η, often referred to as mass vertical coordinate [26]. The coordinates are represented by levels with the purpose of following the topography of the land surface, minimizing the error of surface boundary conditions. To achieve highest resolution near the ground, the levels are quasi-horizontal with the distribution exponentially increasing towards the surface to adjust to small-scale changes in topography. In the WRF model the vertical coordinates are defined by:

$$\eta = \frac{p_d - p_t}{p_s - p_t} \qquad (3.1)$$

Where p_d is the hydrostatic pressure component of dry air, p_s is the pressure value along the surface, and p_t referrers to the pressure value at the top of the model domain.

The value of η varies from 0 at the top of the model domain to 1 at the surface. An example of such a coordinate system is shown in Figure 3.4. The grey area represent the landscape topography, while the pressure value is given by the vertical axis. Both the number of eta-levels and their distribution is user-specified in the WRF model.

In this thesis the number of vertical eta levels are set to 40, but no specific eta levels are chosen. Thus, letting the real program choose the most suitable levels.
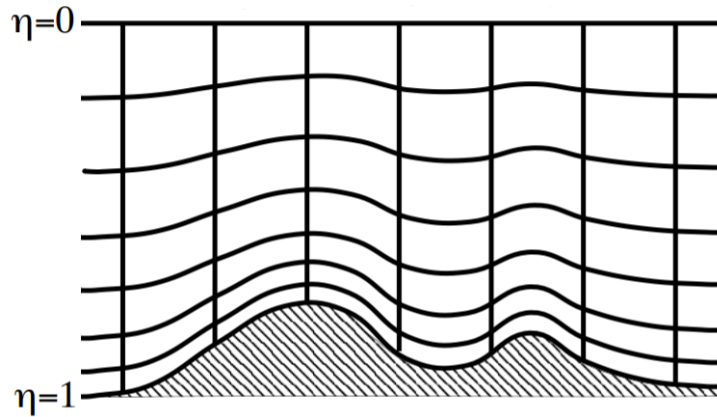
Figure 3.4: η coordinate system used in ARW *[26]*

3.2.4 Map projections

Four map projections are supported by the ARW solver; the polar stereographic, Lambert conformal, Mercator, and latitude-longitude projections [26]. For the first three of the projections; the polar stereographic, Lambert conformal, and Mercator, the transformation is isotropic, which means the orientations along the earth's sphere is uniformity all over the grid: $\frac{\Delta x}{\Delta y}\Big|_{Earth}$ = constant.

No map projection perfectly preserves all properties of the spherical surface of the earth, but instead each of these map projections are best suited at particular latitudes, due to their ability to minimize distortion at these latitudes. As a general rule, the Polar stereographic projection is best suited for domains located at high latitudes, the Mercator projection is well suited for domains at low-latitudes, and the Lambert conformal projection is best suited at mid-latitudes.

Havøygavlen wind park site is located at the latitude 71 degrees north, a very high latitude close to the North pole, making the Polar stereographic projection the obvious choice for this study. The polar stereographic projection uses a projection grid which intersects with the surface of the earth at a so-called true latitude, a real value that can be specified in the pre-processing of the model [27]. At this given latitude the distance in the projected map has true scale, meaning no distortion. Figure 3.5 (a) shows a Polar stereographic projection designed so that the projection grid intersects with the surface at 60 degrees latitude. Due to true scale mapping at the point of intersection there is also no distortion at the pole. As the latitude decreases each grid cell covers more of the Earth's surface, leading to an increase of distortion. An example of such a grid is shown in Figure 3.5 (b).

(a) **(b)**
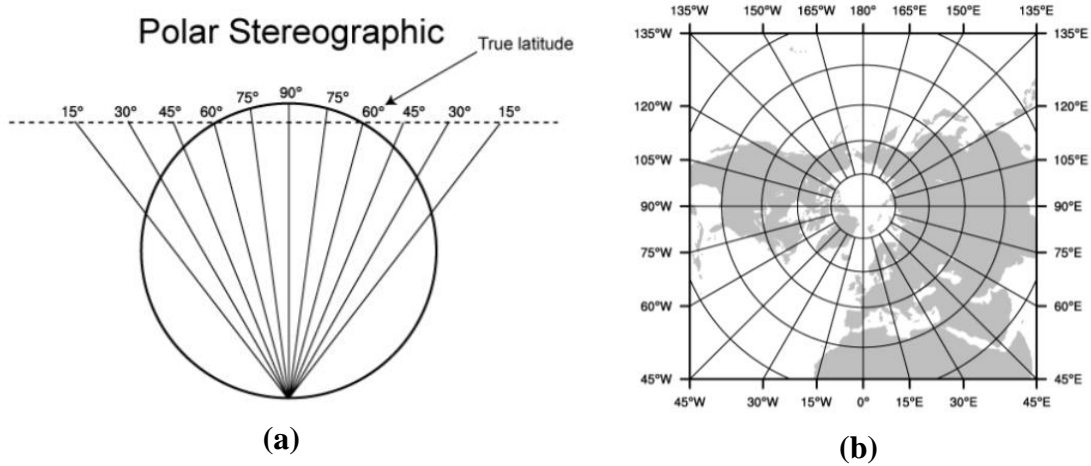
Figure 3.5: (a) Polar stereographic projection designed so that the projection grid intersects with the surface at 60 degrees latitude. (b) Example of a Polar stereographic projection grid. Both figures were obtained from *[27]*.

3.2.5 Numerical methods

Integration scheme option

The WRF model has two available time integration schemes; the 2nd order Runge-Kutta method (RK_2) and 3rd order Runge-Kutta method (RK_3). The recommended and default scheme in the ARW solver is the RK3 [28]. Atmospheric models consist of slow and fast

processes that co-exist, leading to motions with multiple time scales [29]. Principally, RK3 is used to integrate low and medium frequency modes of meteorological importance, such as simple advection, gravity waves and Rossby waves over smaller time steps. To achieve a stable numerical integration the iteration of high frequency acoustic nodes are executed over smaller time steps. This method is called a time-split integration scheme [26], and is implemented as a form of prediction-correction to the integration done by the RK3. According to Wicker and Skamarock [30] this formulation allows for the best combo of simplicity and efficiency for the integration of a compressible nonhydrostatic atmospheric model.

Time step constraint

The numerical iteration done by RK3 require a user-defined time step Δt. The time step must be determined for the purpose of achieving an efficient integration, whilst still be limited to the extent where the information has sufficient time to propagate through the discretization space. the Courant–Friedrichs–Lewy (CFL) condition is a condition that restricts the time step for achieving convergence while numerically solving the differential equations. The CFL condition must be satisfied for a stable solution, but the actual case may require additional restrictions to suffice stability [31].

The CFL condition has the following form for a one-dimensional wind simulation case:

$$C = \frac{u\Delta t}{\Delta x} \leq C_{max} \qquad (3.2)$$

Where C is the Courant number, u is the horizontal wind speed, Δx is the spatially discrete grid spacing, and C_{max} is the maximum stable courant number.

The order of discretization for the advection terms is also user-defined in the ARW solver, and the available alternatives are 2nd through 6th order [26]. Each order affects the maximum stable Courant number, and the user's choice should preferably be the order tolerating the highest courant number while stable, which ultimately allows a larger RK3 time step.

Wicker and Shamarock [30] tested the time step limitations of one-dimensional advection in the RK3 using 4th, 5th and 6th order spatial discretization schemes. The results of their testing

are reproduced in Table 3.1. The table also contain corresponding testing for other time iteration schemes, which demonstrates the performance difference of each scheme.

Time Scheme	Spatial order			
	3rd	4th	5th	6th
Leapfrog	Unstable	0.72	Unstable	0.62
RK2	0.88	Unstable	0.30	Unstable
RK3	1.61	1.26	1.42	1.08

Table 3.1: Time step limitations of one-dimensional advection in the RK3 using 4th, 5th and 6th order spatial discretization schemes. Results are obtained from *[30]*.

To obtain the maximum Courant numbers for three-dimensional advection, the Courant numbers in Table 3.1 must be multiplied by a factor of $1/\sqrt{3}$. By implementing this factor to eq. (3.2) and solving for the maximum stable time step Δt_{max} we obtain:

$$\Delta t_{max} \leq \frac{\Delta x}{\sqrt{3}} \frac{C_{max}}{u_{max}} \tag{3.3}$$

Where C_{max} indicates the maximum Courant number produced in table 3.1, u_{max} is the maximum horizontal wind speed that can be expected during the simulation period, and Δx is the spatially discrete grid spacing of the coarsest simulation domain.

As indicated in table 3.1, the 5th order advection scheme allows the largest stable maximum Courant number, which enable a larger time step than the other advection scheme orders. The simulation executed in this thesis uses the 5th order advection scheme for this purpose. The extent of the vertical domain in the simulation may include polar front jet streams travelling in the tropopause. A scenario where such jet streams approaches velocities of 100 m/s is entirely plausible, and for that reason we assume $u_{max} \approx 100m/s$. The largest grid spacing used in this thesis is the coarsest domain grid spacing of 25 000 meters. As a safety buffer, partly due to the additional restrictions caused by the time splitting scheme, it is common to reduce the time step by approximately 25% [26]. By implementing these values to eq. (3.3) we obtain the following estimation of the maximum time step:

$$\Delta t_{max} \leq \frac{\Delta x}{\sqrt{3}} \frac{C_{max}}{u_{max}} \cdot 75\% = \frac{25000\ m}{\sqrt{3}} \frac{1{,}42}{100 \frac{m}{s}} \cdot 75\% \approx 154\ s \qquad (3.4)$$

For the ARW, a rule of thumb when choosing the time step is letting it be approximately 6 times the grid distance in kilometers, in this case 150 s. In this thesis, the time step chosen for the outermost domain D01 simulation was 150 s.

Truncation error and spin-up time

The numerical iteration scheme used in the WRF-model is an approximation to mathematical formulas that represent actual and exact conditions. After a relatively long iteration time the inaccuracy of the iteration scheme may cause a snowball effect, ultimately accumulating truncation errors. A method to minimize divergence of the prediction model is to perform the simulation in segments, that jointly complete the whole simulation period [32].

Prior to generating future condition estimates the iteration scheme also require boundary conditions and initial conditions. There will always exist some intrinsic problems such as inaccuracy in the observational data used to determine the initial state of the weather prediction model. after being initiated from these conditions, the iteration scheme attempts to stabilize and reach its climatology where trustworthy results are iterated. This time period is called the spin-up time and results calculated before the model has stabilized may be unreliable, and should preferably be avoided.

In this thesis, to minimize the effect of truncation error the simulation period has been segmented into 52 independent simulations representing each week of 2017. The iteration is initiated the last day of 2016, and is reinitialized every 8 days, where the first day, presumably containing the spin-up effects, is discarded. Each reinitialization overlaps the previous segments by 1 day, using the last day of the previous segment for research for further iteration. This is accomplished by interpolation between the overlapping time series, with the purpose of achieving smooth transitions between each segment. Appendix C illustrates a simplified script in MATLAB used to perform the above-mentioned interpolation between segments.

In terms of minimizing possible truncation error in the model, the WRF model also has the option of using grid-nudging techniques on the simulation [26]. The technique is also called Newtonian relaxation, and is part of the four-dimensional data assimilation (FDDA) system of the WRF model. The purpose of the method is to run the model with additional nudging for water vapor, temperature and horizontal wind components, thus forcing each grid point towards a value which has been time-interpolated from analysis. In this thesis, it has been presumed that the techniques mentioned earlier in this section sufficiently minimizes truncation error. Hence, no additional nudging has been implemented.

Extracting wind data at points of interest

In this thesis each of the Havøygavlen wind farm's 16 wind turbines are the points of interest. Horizontally, these points are interpolated by extracting the simulated wind data at the nearest grid indexes of the model domain that coincide with the specific latitude and longitude location of each wind turbine.

The horizontal wind components produced by the WRF-ARW model are standardized at an altitude of 10 meters above the surface of the ground, or averaged to mass points. In order to extract the wind components at the hub height of 80 meters, a vertical interpolation was performed on the horizontally interpolated wind data. This entire procedure is carried out by using in-built functions within the NCAR command language (NCL) [33]. Appendix D illustrates a simplified script of how to extract the data at points of interest using NCL functions.

3.2.6 Physical options

The WRF model offers several physical options which can be chosen in various combination to best suit the particular simulation experiment at hand. Since the WRF Model Version 3.9 update introduced on April 17, 2017, a new way of configuring physical options was implemented by using 'physics_suite' in the WRF namelist [34]. The suite specification 'CONUS' is used in this thesis without any overwrite, and include the following physical options:

- Microphysics option = Thompson scheme

- Cumulus option = Modified Tiedtke scheme

- Longwave radiation option = rrtmg scheme

- Shortwave radiation option = rrtmg scheme

- boundary-layer option = Mellor-Yamada-Janjic (Eta) TKE scheme

- surface-layer option = Monin-Obukhov (Janjic Eta) Similarity scheme

- land-surface option = Noah Land-Surface Model

The 'CONUS' suite selection is established as a result of real-time forecasting analyses over several years over the continent of North America.

3.3 Statistical methods

3.3.1 Correlation between data

Given a vector **x** with finite a number of finite outcomes x_1, x_2, ..., x_k that occur with probabilities p_1, p_2, ..., p_k, respectively, the theoretical mean or expectation value of **x** is given by the following formula:

$$\boldsymbol{\mu} = E[x] = \sum_{i=1}^{k} x_i p_i = x_2 p_2 + x_2 p_2 + \cdots + x_k p_k \tag{3.5}$$

The theoretical variance of the same vector **x** can then be defined as:

$$\boldsymbol{\sigma^2} = var(x) = E[(x - \mu)^2] \tag{3.6}$$

Standard deviation is a measurement of dispersion relative to its mean, and can simply be expressed as the square root of the variance:

$$\sigma = \sqrt{var(x)} = \sqrt{E[(x - \mu)^2]} \qquad (3.7)$$

The covariance between two jointly distributed datasets **X** and **Y** is a measurement of their joint variability and is expressed as:

$$\sigma_{XY} = cov(X, Y) = E\big[(X - \mu_x)(Y - \mu_y)\big] \qquad (3.8)$$

The correlation coefficient between datasets **X** and **Y** is a measurement of the correlation, or the linear relationship between them. The resulting coefficient is a measure of the strenght of both the directional and correlating relationship between the datasets, and is defined as the covariance of the given datasets divided by the product of their standard deviation:

$$p_{XY} = \frac{\sigma_{XY}}{\sigma_X \sigma_Y} = \frac{E\big[(X - \mu_x)(Y - \mu_y)\big]}{\sigma_X \sigma_Y} \qquad (3.9)$$

The attained value is normalized to unity, meaning a perfect degree of correlation would result in a value of ±1, and a value of zero indicates no correlation.

3.3.2 Bias

The tendency of a dataset **X** compared to a dataset **Y** can be assessed by finding the difference of each corresponding data sample. The bias represent the average difference between all these corresponding data samples, and expresses an over or underestimation denoted by a positive or negative resulting value. The bias can be expressed as:

$$Bias = \frac{1}{k} \sum_{i=1}^{k} (X_i - Y_i) \qquad (3.10)$$

E.g., by denoting **X** as the estimation dataset, and **Y** as the observed dataset, a positive bias represent an overestimation by **X** relative to **Y**, while a negative bias indicate an underestimation of the observed data.

3.3.3 RMSE

The root mean square error (RMSE) between datasets **X** and **Y** is a measurement of the difference between their values, and can be expressed as:

$$RMSE = \sqrt{\frac{1}{k}\sum_{i=1}^{k}(X_i - Y_i)^2}$$

(3.11)

RMSE is often used to measure how good a predictive model is over actual observed data. The smaller RMSE value the better accuracy of the model.

3.3.4 Wind rose

Meteorologists often use wind roses as graphic tool to concisely visualize how the speed and direction of the wind is distributed at specific locations [35]. The wind rose is displayed as a circular arrangement showing the frequency of winds that blows in specific directions.

The magnitude of each "petal" is decided by the amount of wind blowing in that direction, and each concentric circle corresponds to particular frequencies starting at zero at the center and gradually increases through the outer circles. The speed of the wind is visualized by the colouring of each section of each "petal". In this thesis the direction of the wind will be interpreted as the direction from which it originates from, e.g., from where it's blowing from.

An example of a wind rose is shown in figure 3.4. The compass is divided into 16 section of 22,5 degrees each, and every wind direction within this section determines the frequency in this particular direction. The wind rose displays the relative rate of occurrence of wind from one specific point through a whole year. It also indicate a prevailing wind originating around the NE, and the most dominant direction where high wind speeds above 20 m/s occurs, originates at ENE.
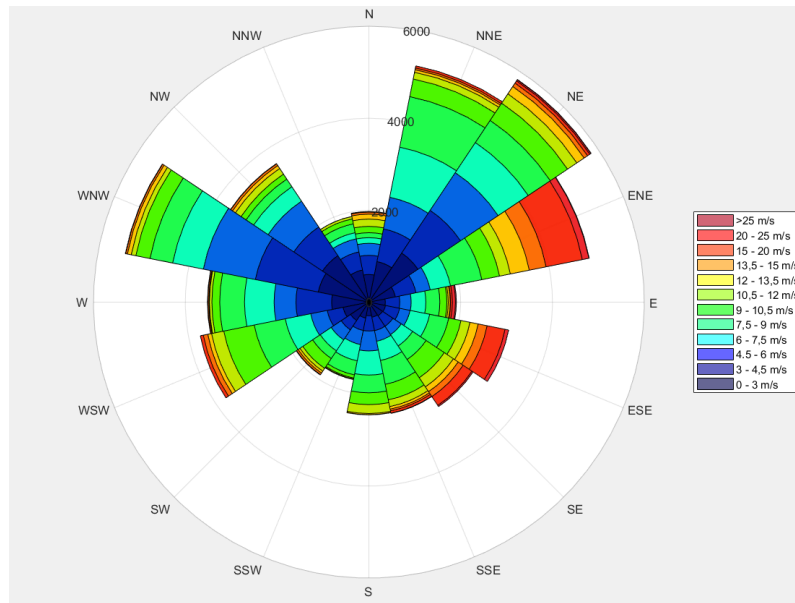
Figure 3.6: Example of a wind rose.

3.3.5 Average wind map

In order to map the wind resources surrounding Havøygavlen, average wind mapping will be used. Since on-site measurements only account for specific geographical points, the WRF model is advantageously able to facilitate the wind resources of an entire region averaged over a period of time. Figure 3.7 illustrates the average wind speed at each grid point of D03 interpolated to hub height of 80 meters, for the first week of 2017. The map is created using an NCL-script, which firstly calculates the wind speed at 80 meters for each grid point at each time step of 10 minutes, and secondly averages the wind speed over a given time period by finding the arithmetic mean of these values. The map is finally displayed by a contour plot, where each wind speed corresponds to a colour assign by a panel. Additional contour lines signifying topography within the domain is also included in the figure. Here, the contour interval are set to 100 meters.
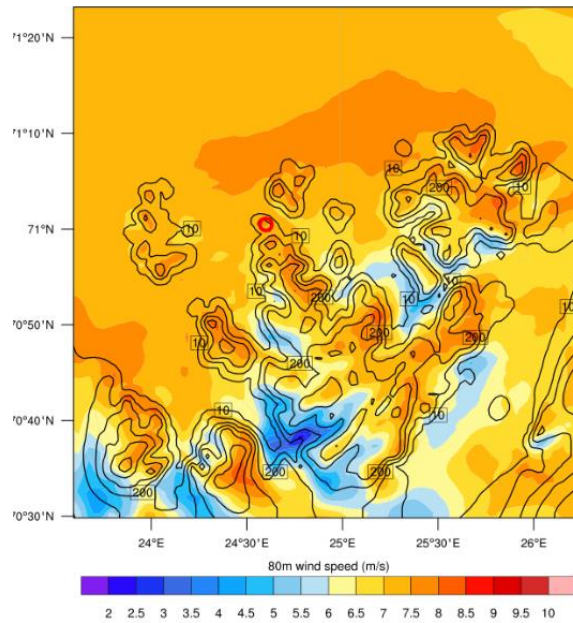
Figure 3.7: Weekly average wind speed map at 80 meters covering the area confined by D03 in the first week of 2017.

This thesis will focus on mapping the annual wind speed at 80 meters for both D02 and D03. This is achieved by attaching every wind speed array within all segments corresponding to each week of 2017, as mentioned in section 3.3.3. The first day of each segment is similarly discarded to reduce the effect of spin-up, leading to a continuous transition between adjacent segments. Each grid point, now containing wind speeds for the entirety of 2017, is then average and mapped equivalently to the weekly average wind speed map displayed in Figure 3.7. A simplified NCL-script used to produce an annual mean wind speed map over D03 is appended in Appendix E.

3.3.6 Box plot

A box plot is a graphical method used to describe groups of data through displaying the data quartiles and averages [36]. Figure 3.8 displays a box plot example where the different components of the plot is annotated. The boundaries of the box is determined by the interquartile range set by the lower quartile, signifying the boundary line for which 25 percent of the data values fall beneath, and the upper quartile signifies the boundary line for which 75 percent of the data values fall below. The red line in the middle of the box indicate

the median of the data, meaning half the values fall below this line, and half the values are above it. The whiskers at each side of the box indicate the maximum and minimum value of the data, respectively. The spacing between all mentioned parts can indicate the extent of dispersion and skewness within datasets.
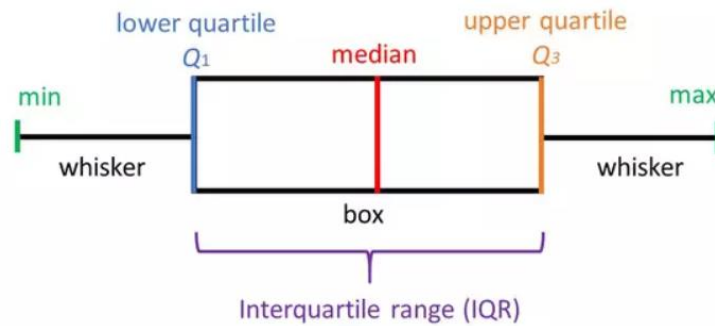
Figure 3.8: Explanatory box plot example *[36]*.

4 Result and discussion

In this chapter the result from the WRF simulation will be compared to on-site measurements conducted at hub height of each wind turbine at Havøygavlen wind farm site. The estimated data used in comparison will mainly be collected from D03 at points interpolated to the respective turbine locations. Wind speed and wind direction at these points for both observed data and estimated data will be displayed using wind roses and various graph types. An assessment of the wind resources for the entirety of D02 and D03 will be displayed using annual mean wind maps. Additionally, the performance of all simulations will be established by statistical methods presented in chapter 3.3. Here, D02 will be evaluated in conjunction with D03 for the sake of comparison. All presented results will later be discussed and evaluated.

4.1 Observed data

The annual distribution of wind speed measured at hub height of each turbine at Havøygavlen in 2017 is displayed as normalized histograms in Figure 4.1 (a)-(p), in addition to the annual mean wind speed. Due to the natural zero limit of the measurements all distributions are right-skewed, but some dissimilarities amongst the turbines can be observed. By inspecting the geographical placement of each windmill at Havøygavlen in Figure 1.1, all clear bimodal distributions seem to occur in the northwest, at the edge of the park. Although there are some exceptions, the general tendency indicate that this second peak plateaus towards the southeast of the site, before eventually appearing unimodal.

The originating direction of the wind arriving at the site may be the reason for multiple peaks in the probability distribution. The complex terrain shorewards hinders the wind, which lowers the occurrence of higher wind speeds, while wind originating from the ocean has clearer path towards the site. As a result, turbines situated on the edge of the island are

more well-equipped for capturing these higher wind speeds. In terms of annual mean wind speed, there is no apparent locational tendency among the turbines.

However, the turbines with the lowest measured mean wind speeds are mostly centrally situated, and the highest measured mean wind speed tend to be part of the northernmost row.
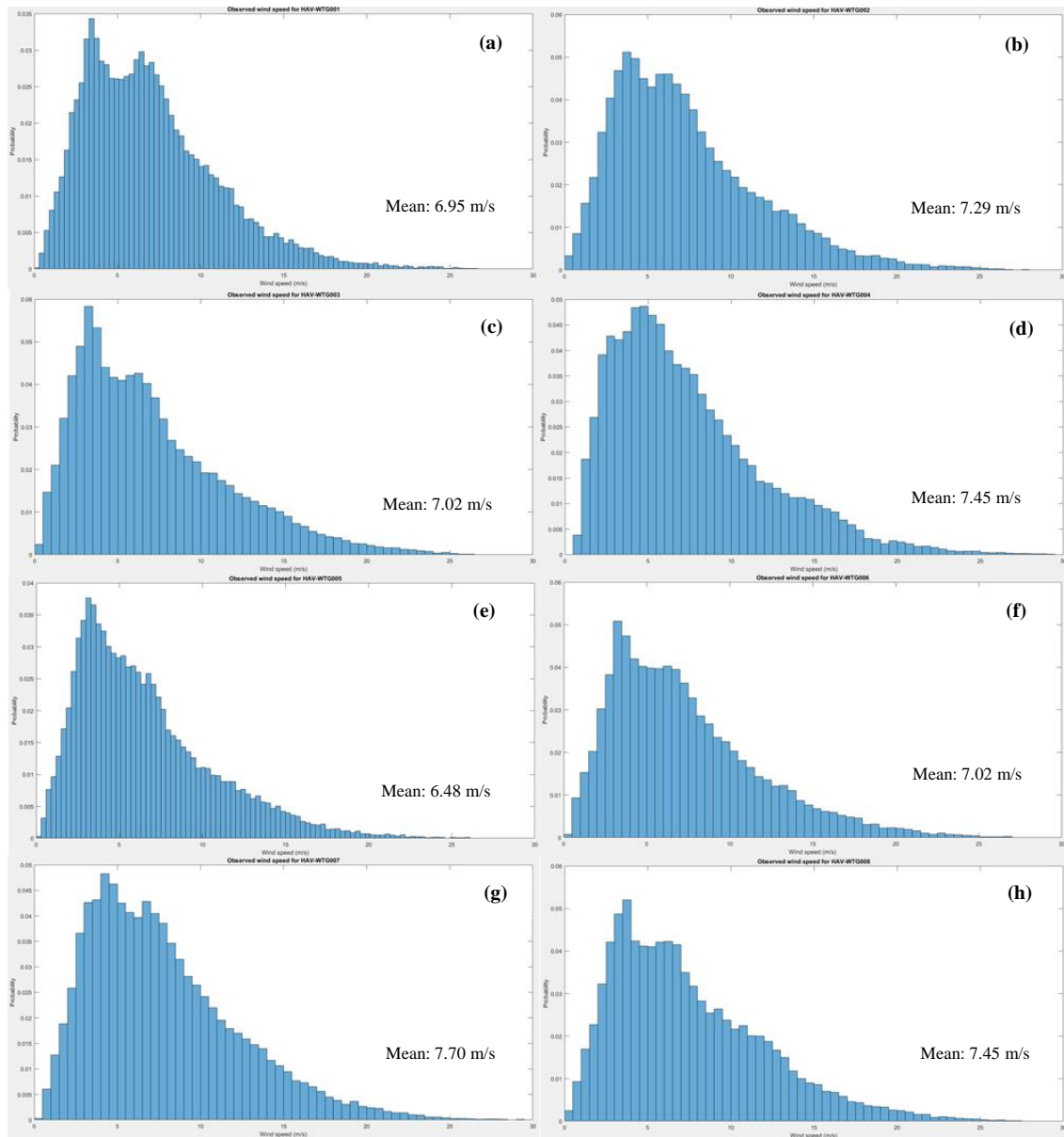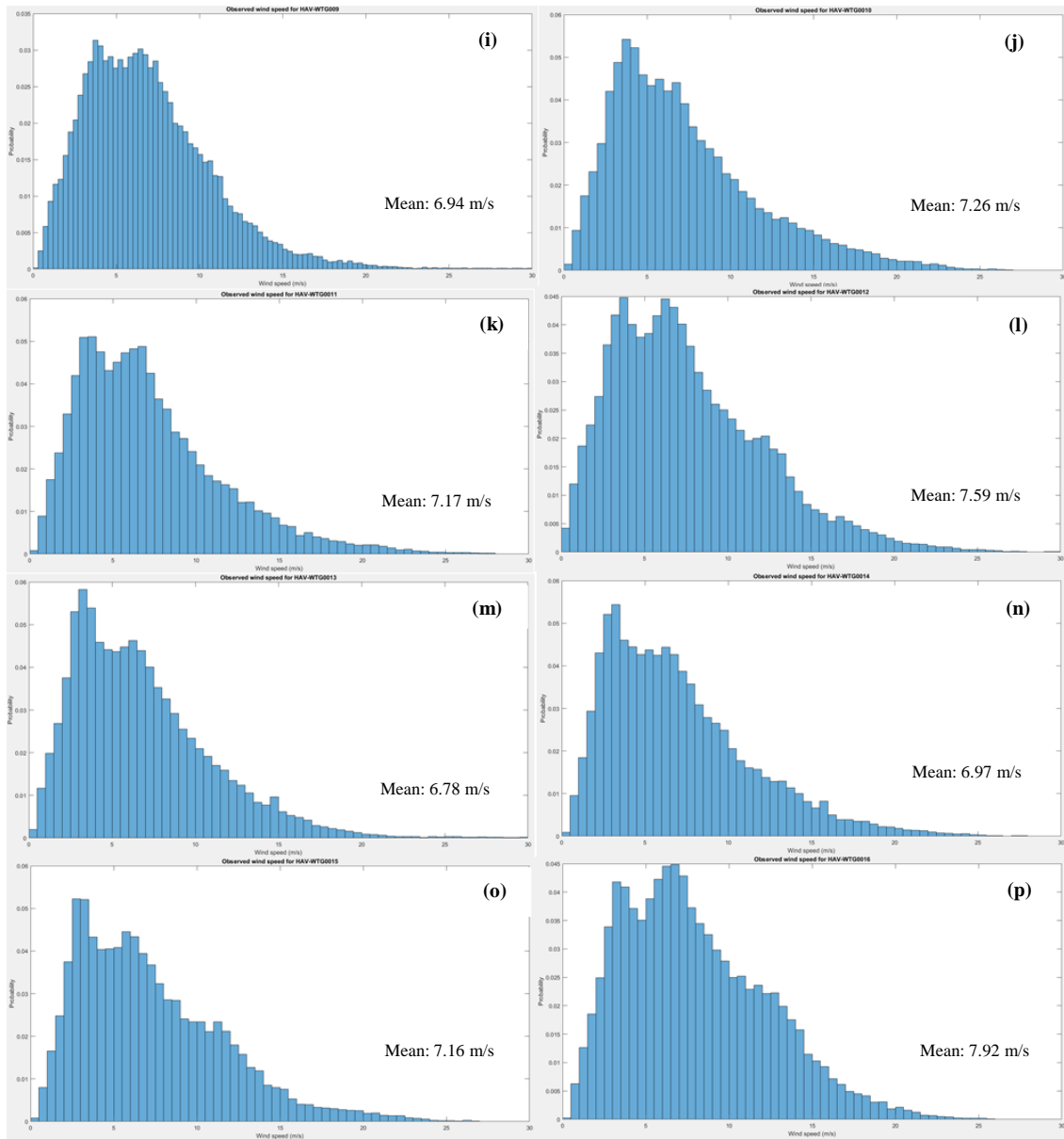
Figure 4.1: (a)-(p) Normalized histograms showing the wind speed distribution through 2017 for each wind turbine, respectively. The annual mean wind speed for each turbine is also included.

As mentioned in section 3.1.1, the only trustworthy directional on-site measurements came from HAV-WTG004. The available measurements for this turbine only span from about 24. October until the end of the year. All measurements are done at 80 meters height. The directional degree of each sample is plotted as a function of time in Figure 4.2 (a), while Figure 4.2 (b) plots each wind speed sample as a function of direction for the same time period. The plots indicate a prevailing wind originating around 200-250 degrees, which coincide with a southeast origin. The same evidence is found in Figure 4.3 (a) displaying the same measurements in a wind rose. Figure 4.3 (b) is placed alongside the wind rose, and compose of a satellite image enclosed by a compass centred at the wind farm site to emphasise the course of the wind. The green square pinpoint the location of HAV-WTG004, while all other turbines at the site are mark with red dots.
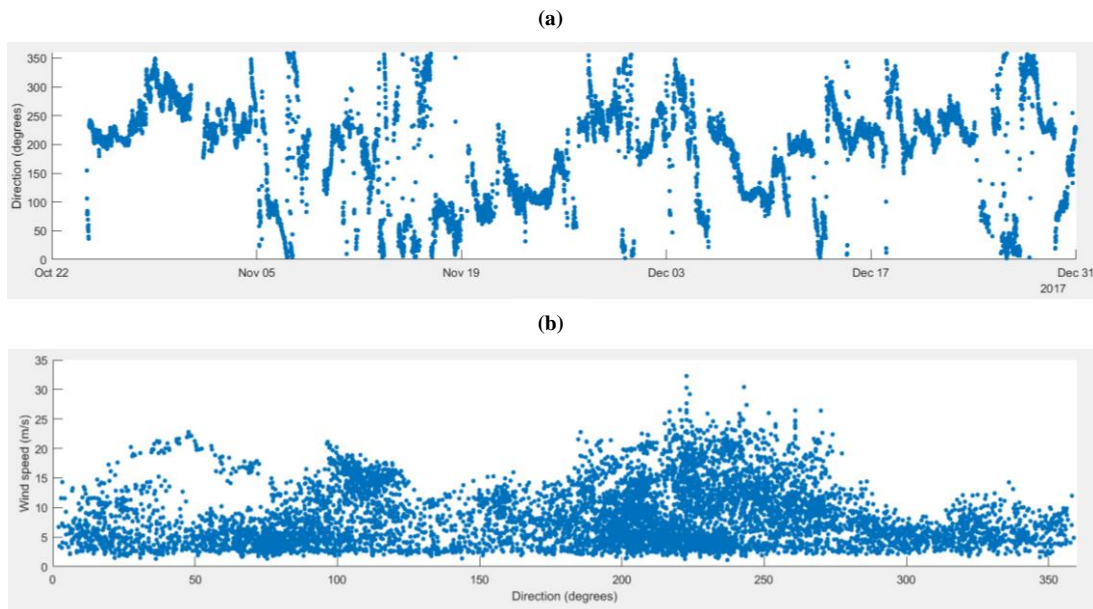
Figure 4.2: (a) Plot of measured wind direction as a function of time for HAV-WTG004. (b) Plot displaying comparison of measured wind speed and wind direction in corresponding time period.
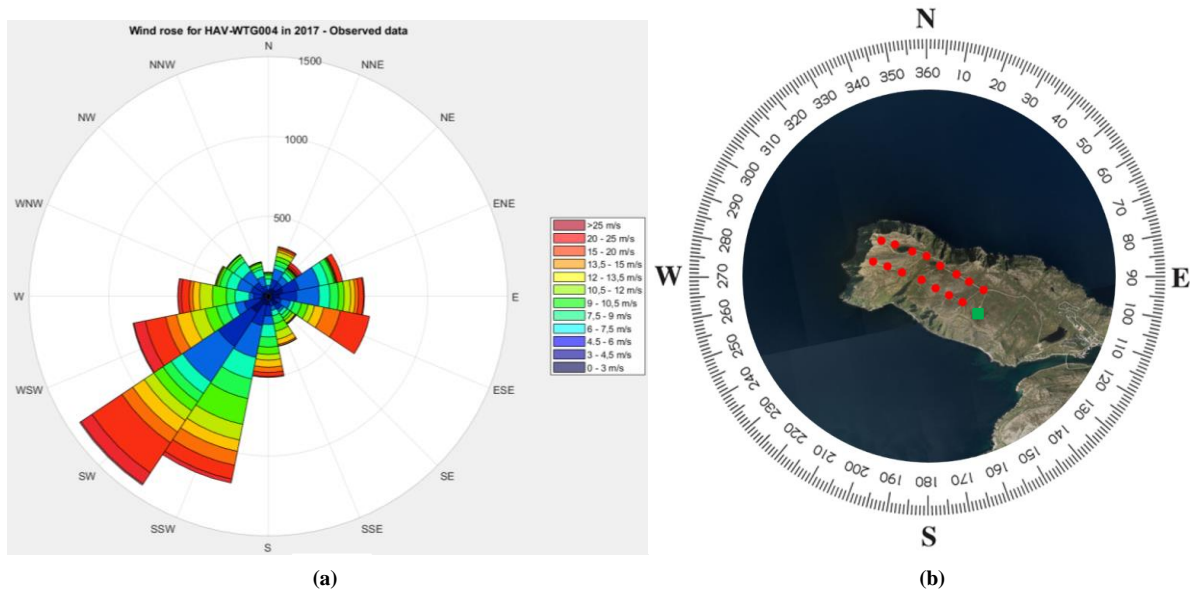
Figure 4.3: (a) Wind rose displaying wind direction for HAV-WTG004 measured at 80 meters in the time period 24.10.17-31.12.17. (b) Directional description of the wind park. green square mark the location of HAV-WTG004, while all other turbines at the site are mark with red dots. Satellite image is gathered from norgeskart.no.

4.2 WRF simulation

The WRF simulation was run for the whole of 2017. The Namelists appended in Appendix B constitute a summary of the WRF model setup used on each segment of the simulation period. Extraction of data at the location of each wind turbine was performed using the script appended in Appendix D, while all segments where patch up through interpolation in each overlap transition using the script appended in Appendix C. All data presented in this section is either measured or interpolated to hub height of 80 meters.

4.2.1 Wind speed analysis

The RMSE, Correlation and Bias between on-site measurements and the two innermost WRF domains for each turbine situated at Havøygavlen are displayed in Table 4.1. For HAV-WTG004, both horizontal wind speed and wind direction are compared, while for the rest of the turbines, only a comparison of horizontal wind speed is included due to the wind direction measurements performed by the Nordex N80 windmills not being dependable.

For each turbine, Table 4.2 present the mean wind speed measured on-site, as well as the WRF estimated mean wind speed for the two innermost domains, respectively. All tabulated results are divided into months of 2017, so that the seasonal variations are emphasised, in addition to an annual total.

Regarding to the comparison of on-site measurements and the two innermost domains of the WRF simulation, no apparent performance enhancement can be detected for D03 relative to D02. As a matter of fact, D02 has the highest correlation coefficient and lowest RMSE for all months of the simulation period. Considering the bias of the estimator, D03 performs better than D02, being less bias for every month of the simulation. The same predictive tendency can be found for the wind direction parameter, exclusively examined for HAV-WTG004, although D03 also has the highest bias regarding wind direction. As the bias of an estimator offsets positive errors with negative errors, a lower bias does not necessarily indicate a more precise estimation. RMSE is a measure of the average magnitude of the error, implying a higher weight on larger errors. Summed up, this suggest that D03 fails to enhance the accuracy of the forecast with respect to D02.

Wind turbines	Statistical methods	Domain	
		D02	D03
HAV-WTG001	RMSE wind speed (m s⁻¹)	4.66	4.81
	Correlation wind speed	0.288	0.281
	Bias wind speed (m s⁻¹)	-0.9142	-0.3463
HAV-WTG002	RMSE wind speed (m s⁻¹)	4.99	5.08
	Correlation wind speed	0.287	0.283
	Bias wind speed (m s⁻¹)	-1.2613	-1.1269
HAV-WTG003	RMSE wind speed (m s⁻¹)	5.04	5.15
	Correlation wind speed	0.286	0.277
	Bias wind speed (m s⁻¹)	-0.9833	-0.8561
HAV-WTG004	RMSE wind speed (m s⁻¹)	5.13	5.30
	Correlation wind speed	0.304	0.360
	Bias wind speed (m s⁻¹)	-1.2213	-1.1412
	RMSE wind direction (°)	82.84	90.56
	Correlation wind direction	0.404	0.318
	Bias wind direction (°)	14.21	16.31
HAV-WTG005	RMSE wind speed (m s⁻¹)	4.63	4.85
	Correlation wind speed	0.282	0.274
	Bias wind speed (m s⁻¹)	-0.4253	- 0.1381
HAV-WTG006	RMSE wind speed (m s⁻¹)	5.05	5.15
	Correlation wind speed	0.289	0.285
	Bias wind speed(m s⁻¹)	-1.2490	- 0.6836
HAV-WTG007	RMSE wind speed (m s⁻¹)	5.19	5.26
	Correlation wind speed	0.280	0.271
	Bias wind speed (m s⁻¹)	-1.6437	- 1.0918
HAV-WTG008	RMSE wind speed (m s⁻¹)	5.20	5.32
	Correlation wind speed	0.283	0.279
	Bias wind speed (m s⁻¹)	-1.3970	- 1.1287

HAV-WTG009	RMSE wind speed (m s^{-1})	4.63	4.79
	Correlation wind speed	0.289	0.284
	Bias wind speed (m s^{-1})	-0.8615	- 0.2983
HAV-WTG010	RMSE wind speed (m s^{-1})	5.02	5.13
	Correlation wind speed	0.290	0.282
	Bias wind speed (m s^{-1})	-1.2005	- 0.6396
HAV-WTG011	RMSE wind speed (m s^{-1})	4.92	4.97
	Correlation wind speed	0.290	0.277
	Bias wind speed (m s^{-1})	-1.1225	- 0.5976
HAV-WTG012	RMSE wind speed (m s^{-1})	5.12	5.13
	Correlation wind speed	0.299	0.282
	Bias wind speed (m s^{-1})	-1.5652	- 1.0440
HAV-WTG013	RMSE wind speed (m s^{-1})	4.68	4.84
	Correlation wind speed	0.300	0.294
	Bias wind speed (m s^{-1})	-0.7016	- 0.1356
HAV-WTG014	RMSE wind speed (m s^{-1})	4.94	5.04
	Correlation wind speed	0.277	0.268
	Bias wind speed (m s^{-1})	-0.9607	- 0.4530
HAV-WTG015	RMSE wind speed (m s^{-1})	4.92	5.00
	Correlation wind speed	0.290	0.284
	Bias wind speed (m s^{-1})	-1.0896	- 0.5902
HAV-WTG016	RMSE wind speed (m s^{-1})	5.13	5.13
	Correlation wind speed	0.295	0.288
	Bias wind speed (m s^{-1})	-1.9064	- 1.4013
Average for site	RMSE wind speed (m s^{-1})	4.95	5.06
	Correlation wind speed	0.289	0.268
	Bias wind speed (m s^{-1})	-1.1564	-0.7295

Table 4.1: RMSE, Correlation and Bias between on-site measurements and the two innermost WRF domains.

Months	HAV-WTG001 Mean wind speed (m s^{-1})			HAV-WTG002 Mean wind speed (m s^{-1})			HAV-WTG003 Mean wind speed (m s^{-1})			HAV-WTG004 Mean wind speed (m s^{-1})		
	On-site	D02	D03	On-site	D02	D03	On-site	D02	D03	On-site	D02	D03
January	10.14	8.59	9.45	10.52	8.62	9.03	10.56	8.62	9.03	10.26	8.64	9.08
February	6.36	8.59	9.41	6.20	8.58	9.00	6.05	8.58	9.00	7.56	9.52	10.11
March	8.37	9.84	10.86	8.79	9.84	10.41	8.38	9.84	10.41	8.77	9.95	10.26
April	6.06	4.36	4.83	6.39	4.36	4.55	6.01	4.36	4.55	6.47	4.35	4.35
May	6.72	4.78	5.23	7.33	4.78	4.91	6.83	4.78	4.91	6.82	4.78	4.78
June	6.23	6.97	7.50	6.57	6.97	6.70	6.26	6.97	6.70	6.81	6.97	6.82
July	6.08	4.51	5.22	6.35	4.51	4.59	5.82	4.52	4.59	6.32	4.46	4.59
August	5.43	5.54	6.03	5.95	5.54	5.76	5.45	5.54	5.76	5.79	5.44	5.65
September	6.09	5.47	6.17	6.57	5.47	5.70	6.59	5.52	5.67	6.69	5.59	5.78
October	7.40	4.50	4.87	7.71	4.50	4.29	7.50	4.50	4.29	8.20	4.88	4.54
November	6.18	4.94	5.12	6.63	4.94	4.89	6.34	4.94	4.88	6.76	4.93	4.68
December	8.37	5.75	6.01	8.50	5.75	5.77	8.40	5.75	5.77	8.89	5.75	5.67
Total	6.95	6.15	6.73	7.29	6.15	6.30	7.02	6.16	6.30	7.45	6.27	6.36

Months	HAV-WTG005 Mean wind speed (m s^{-1})			HAV-WTG006 Mean wind speed (m s^{-1})			HAV-WTG007 Mean wind speed (m s^{-1})			HAV-WTG008 Mean wind speed (m s^{-1})		
	On-site	D02	D03	On-site	D02	D03	On-site	D02	D03	On-site	D02	D03
January	9.75	8.61	9.48	10.93	8.63	9.50	10.68	8.63	9.50	11.24	8.51	9.03
February	5.86	8.58	9.41	6.40	8.58	9.41	6.80	8.57	9.40	6.31	8.58	8.95
March	7.56	9.83	10.84	8.50	9.85	10.87	9.19	9.84	10.86	8.76	9.84	10.44
April	5.47	4.36	4.83	6.22	4.36	4.83	6.81	4.36	4.83	6.36	4.35	4.55
May	5.79	4.78	5.23	6.67	4.78	5.23	7.43	4.78	5.23	7.02	4.81	4.99
June	5.94	6.97	7.50	6.60	7.02	7.55	7.05	7.00	7.53	6.69	7.03	7.60
July	5.57	4.57	5.27	6.43	4.48	5.18	7.11	4.70	5.41	6.63	4.72	5.21
August	5.14	5.57	6.08	4.41	6.38	7.14	6.18	5.55	6.03	5.90	5.54	5.78
September	6.03	5.40	6.05	5.26	3.37	3.99	7.22	5.40	6.05	7.04	5.52	5.85
October	6.86	4.50	4.87	7.55	4.50	4.87	8.02	4.50	4.87	7.87	4.50	4.57
November	5.88	4.94	5.12	6.66	4.94	5.12	6.97	4.94	5.12	6.77	4.94	4.70
December	7.86	5.75	6.01	8.55	5.75	6.01	8.96	5.75	6.01	8.82	5.75	5.67
Total	6.48	6.15	6.73	7.02	6.05	6.64	7.70	6.17	6.74	7.45	6.17	6.45

	HAV-WTG009			HAV-WTG010			HAV-WTG011			HAV-WTG012		
	Mean wind speed (m s⁻¹)			Mean wind speed (m s⁻¹)			Mean wind speed (m s⁻¹)			Mean wind speed (m s⁻¹)		
Months	On-site	D02	D03	On-site	D02	D03	On-site	D02	D03	On-site	D02	D03
January	10.69	8.63	9.50	10.97	8.57	9.42	10.95	8.63	9.19	11.34	8.42	8.93
February	6.86	8.58	9.41	6.52	8.58	9.40	6.43	8.58	9.13	6.77	8.47	8.99
March	8.19	9.84	10.86	8.54	9.83	10.86	8.47	9.85	10.46	9.47	9.96	10.57
April	5.99	4.36	4.83	5.98	4.36	4.83	6.02	4.36	4.80	6.44	4.33	4.77
May	6.42	4.78	5.23	6.74	4.78	5.23	6.82	4.78	5.21	7.50	4.78	5.21
June	6.15	6.97	7.50	6.52	6.97	7.49	6.58	6.97	7.69	6.70	6.97	7.69
July	5.91	4.52	5.24	6.46	4.52	5.25	6.31	4.51	5.21	6.70	4.48	5.19
August	5.47	5.55	6.03	5.86	5.54	6.03	5.66	5.55	5.89	6.25	5.65	5.97
September	6.41	5.57	6.20	6.76	5.52	6.16	6.63	5.52	6.07	6.91	5.52	6.07
October	6.95	4.50	4.87	7.55	4.50	4.87	7.49	4.50	4.95	7.83	4.50	4.95
November	5.98	4.94	5.12	6.55	4.94	5.12	6.46	4.94	5.37	6.77	4.94	5.37
December	8.20	5.75	6.01	8.61	5.75	6.01	8.17	5.75	6.18	8.39	5.75	6.18
Total	6.94	6.16	6.73	7.26	6.15	6.72	7.17	6.16	6.68	7.59	6.15	6.66

	HAV-WTG013			HAV-WTG014			HAV-WTG015			HAV-WTG016		
	Mean wind speed (m s⁻¹)			Mean wind speed (m s⁻¹)			Mean wind speed (m s⁻¹)			Mean wind speed (m s⁻¹)		
Months	On-site	D02	D03	On-site	D02	D03	On-site	D02	D03	On-site	D02	D03
January	10.06	8.62	9.49	10.39	8.63	9.18	10.62	8.64	9.18	11.27	8.64	9.18
February	6.56	8.58	9.41	6.20	8.58	8.92	5.90	8.58	8.92	6.64	8.58	8.91
March	8.18	9.84	10.86	8.22	9.84	10.55	8.61	9.84	10.55	9.16	9.84	10.55
April	5.72	4.36	4.83	5.97	4.36	4.83	5.93	4.36	4.83	6.65	4.36	4.83
May	6.20	4.78	5.23	6.70	4.78	5.24	6.99	4.78	5.24	7.73	4.78	5.24
June	6.11	6.97	7.50	6.56	6.97	7.97	6.37	7.00	8.00	7.54	6.97	7.97
July	5.81	4.51	5.23	6.22	4.51	5.25	6.94	4.88	5.62	6.93	4.51	5.25
August	5.45	5.55	6.03	5.16	5.37	5.68	5.31	5.52	5.83	6.06	5.54	5.86
September	6.02	5.52	6.16	5.76	5.47	5.99	6.24	5.52	6.02	7.26	5.52	6.02
October	6.61	4.57	4.96	6.89	4.50	5.01	7.28	4.50	5.01	8.22	4.50	5.01
November	6.41	4.94	5.12	6.44	4.94	5.06	6.83	4.94	5.06	7.74	4.94	5.06
December	8.21	5.76	6.02	9.11	5.76	5.93	8.94	5.76	5.93	9.81	5.76	5.93
Total	6.78	6.17	6.74	6.97	6.14	6.63	7.16	6.19	6.68	7.92	6.16	6.65

Table 4.2: Monthly mean wind speed comparison of on-site measurements and WRF estimates for D02 and D03.

Further investigation must be carried out in order to understand why RMSE, bias and correlation coefficient indicate an underperformance of D03. Figure 4.4 (a)-(c) present monthly horizontal wind speed for March, July and November, respectively, comparing on-site data (green line) with estimated data from D03 (red line) and D02 (blue line) for HAV-WTG001 in a conjoint plot. These months are chosen for the purpose of grasping how the WRF estimated domains adapt to the seasonal differences, while HAV-WTG001 is chosen for its operational consistency through the simulation period. Table 4.3 display the RMSE, Correlation and Bias between on-site measurements and the two innermost WRF domains for HAV-WTG001, in March, July and November.

(a)

(b)

Months	RMSE wind speed (m s⁻¹)		Correlation wind speed		Bias wind speed (m s⁻¹)	
	D02	D03	D02	D03	D02	D03
March	5.15	5.64	0.380	0.391	1.46	2.26
July	3.77	3.62	0.33	0.34	-1.63	-1.14
November	5.07	5.16	0.158	0.148	-1.30	-1.20

Table 4.3: RMSE, Correlation and Bias between on-site measurements and the two innermost WRF domains for HAV-WTG001, in March, July and November.

In general, both of the WRF domains compared in Figure 4.4 (a)-(c) tend to underestimate high wind speed and overestimate low wind speed. The same indication can be detected in Table 4.2, where the WRF model only overestimate the mean wind speed in February and March for all 16 turbines. Furthermore, the WRF estimates are more accurate at months of low to moderate mean wind speeds, than months of higher wind speeds.

During the winter months characterized by colder temperatures, the temperature gradient is higher which leads to greater pressure differences. As a result, months with low average temperatures brings higher average wind speeds. Since both D03 and D02 tend to underestimate high wind speed and overestimate low wind speed, negative biases tend to occur in the summer months, and positive biases tend to occur in winter months. Results displayed in Table 4.3 for July and March confirms this discovery.

Despite very similar estimates performed by the two innermost simulations, D03 apt to produce larger local maximas and minimas through all months in question. Particularly in months of high average wind speed such as March, this results in a larger RMSE for D03, due to the statistical method's higher weight on larger errors. Both domains achieve better correlation coefficients in March and July compared to the annual result presented in Table 4.1. The on-site measured wind speed in November contain large variation in magnitude which appears swiftly and abrupt. The poor overall performance displayed from both D03 and D02 on capturing the wind speed measured in this period may imply a deficiency of the model's ability to adjust to these sudden changes in wind speed.

To demonstrate the bias tendencies for WRF estimated wind speeds for each wind turbine at Havøygavlen, a graphical interpretation using scatter plots will be used. These tendencies are displayed in figure 4.5 (a)-(p), using scatter plots for each wind turbine stationed at Havøygavlen, respectively. The scatter plot compares each estimated data sample of D03 to the corresponding observed data sample. All samples of both data sets are results of averaging each day of 2017, for the sake of visual clarity. The y-axis denotes the average wind speed estimated by the daily average wind speed measured by the respective wind turbine, while the x-axis denotes the daily average wind speed estimated by the WRF-model. The red line is a least square regression line with the best fit to the scatter plot, while the green line indicates the linear relationship of an unbiased estimator and the true value of the estimated parameter, in this case being the on-site measurements.

Hence, the closer each point of the scatter plot is to the green line, the better the performance of the estimator. Each point located above the green line indicates an overestimation, while points below the line signifies an underestimation. The slope of the red line displays the WRF-models tendency to underestimate the on-site wind speeds measured at Havøygavlen, due to the more gradual incline compared to the unbiased line. The bias of the WRF-model is displayed in the bottom left corner. Note that this value will deviate slightly from the actual bias of the estimator due the daily averaging applied to the both data sets. A negative bias signifies the WRF-model's underestimation of wind speed in 2017 as a whole.
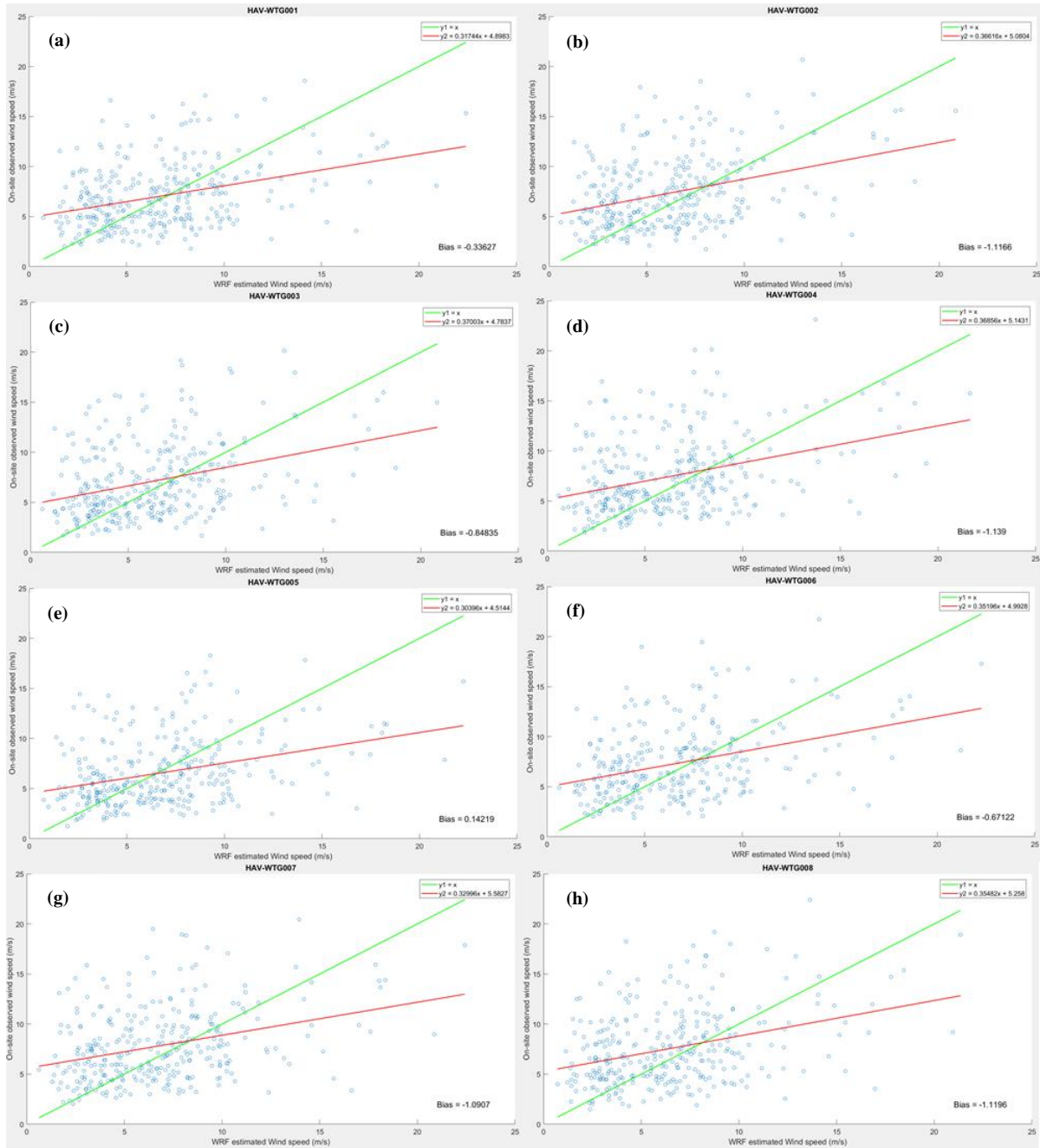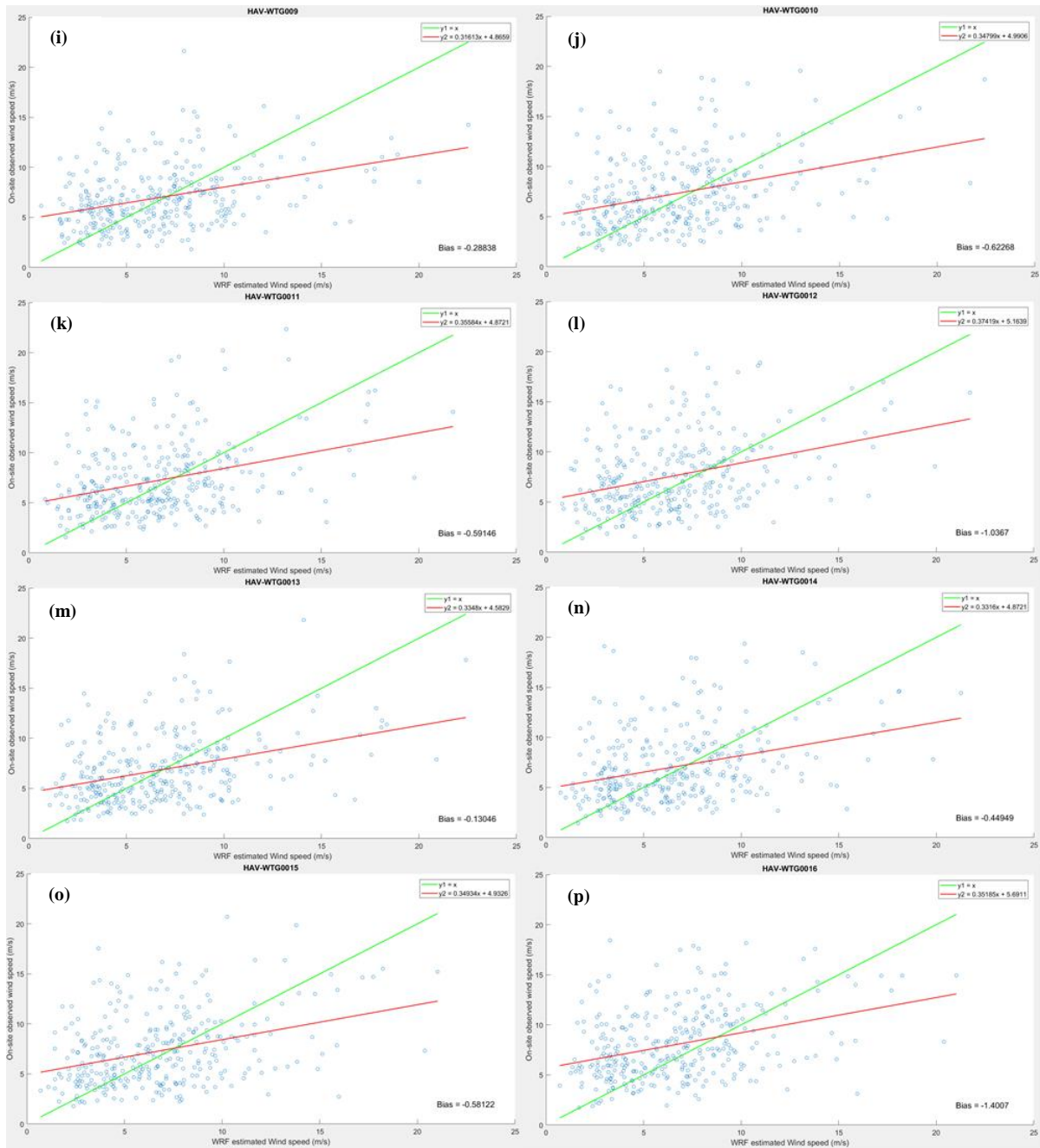
Figure 4.5: (a)-(p) Bias tendency assessment of estimated wind speed for D03 of the WRF-model for each of the 16 wind turbines located at Havøygavlen. The red line is a least square regression line of best fit to the scatter plot, while the green line indicates the scenario of an unbiased estimator.

The performance of all three two innermost domains in estimating the annual mean wind speed is visualized in Figure 4.6. D01 is included to clarify the performance trend between all grid resolutions used in the thesis. The group of data represented by the box plot compose of the annual mean wind speed for each of the 16 wind turbines stationed at Havøygavlen. The red line of each box signify the median, in this case the average of the two middle turbines. The lower quartile, signifying the boundary line for which 4 of the wind turbines fall below, while the upper quartile signifies the boundary line for which 12 of the turbines fall below.

The desired result of displaying the mean wind speed for each turbine as box plots for each domain as well as the observed wind speed, is for the interquartile range to increase parallelly with the domain resolution. Due to the finer resolution of D03, differences in average wind speed within the wind park should be more apparent relative to the coarser resolution of D02 and D01.

By examining Figure 6.1, D01 actually has a greater interquartile range than D02, which does not agree with the predicted result. Both of the coarsest domains does however have very small annual wind speed deviations among the turbines, compared to D03. For D01, one of the turbines differs beyond the maximum whisker length set for the box plot. The extreme data point is considered an outlier, and is plotted as a plus sign in the figure. Due to the low resolution of D01, all turbines are expected to reside within the same grid points, which should result in very similar estimation among the turbines.

D03 shows enhanced performance in estimating the differences in average wind speed within the park, displayed by the larger interquartile range. Furthermore, the figure visualizes the performance enchantment of the finer domain regarding prediction accuracy of the wind resources at the wind park, as the mean wind speed estimates by D03 for each turbine is closer to the on-site measurements, compared to the coarser domains.
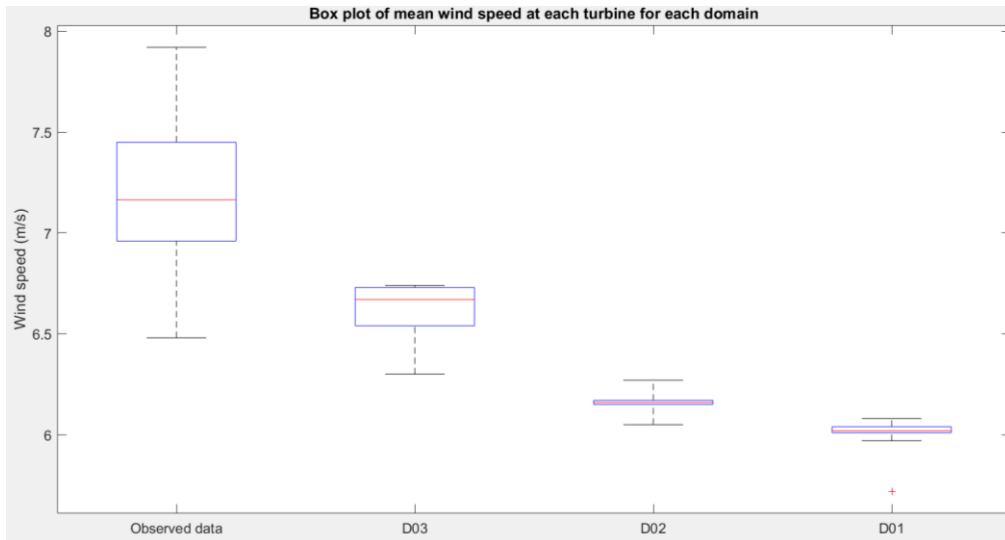
Figure 4.6: Box plot composed of the annual mean wind speed for each turbine at Havøygavlen, in regard to on-site measurements, D03 and D02.

In order to examine why the WRF model struggles to detect differences within the wind park, the average wind speed for each grid indices of D03 and D02 will be displayed in annual mean wind speed maps. Both maps will also be examined in order analyse their performance in capturing the wind resources of each respective domain. The maps are presented in Figure 4.7 (a)-(b) for D02 and D03, respectively, while additional zoomed versions are included in Figure 4.7 (c)-(d) for D02 and D03, respectively. Both zoomed maps covers the same area cropped to 15x15 kilometers of their respective domain, though some inaccuracy in respect to geographical coordinates is unavoidable. Black contour lines signifying topography within the domain is also included. the contour interval are set to 100 meters for Figure 4.7 (a)-(b), and set to 50 meters for Figure 4.7 (c)-(d). It is essential to recognize that the resolution of zoomed maps for each domain is unchanged.

The map demonstrate the terrain's effect on the estimated wind speed. Wind coming in from the open sea is unaffected by terrain which causes the wind to move unhindered, leading to higher estimated wind speeds in this area. The lowest annual mean wind speeds occur where the terrain is roughest, around hilltops and along fjords, where the friction of the surface slows down the air flow.

The smoothened resolution of D02 captures the surrounding terrain poorly compared to D03. However, both D03 and D02 underestimates the complexity of the surrounding topography, as well as the elevation of the plateau where the turbines are situated. As the wind speed

increases with altitude, as mentioned in eq. (2.45), the effect of a smoothened terrain may cause the model to underestimate the wind speed due to an interpolated point of interest at a far lower altitude, than in reality. This may also outweigh the effect of a smoothened topography surrounding the site increasing the estimated wind speed. As demonstrated in Figure 4.6, the median annual mean wind speed measured on-site was approximately 7.2 m/s, which may indicate that the use of an even higher resolution would enhance the model performance of assessing the wind resources of the site.

 The zoomed maps in Figure 4.7 (c)-(d) signifies the differing performance of the two innermost domains in capturing the small variations in annual mean wind speed measured at each respective turbine. D02 displays most of the turbines within the same colour section signifying similar wind speeds, while the plotted turbines in D03 occupies different colour sections. This implies that D03 has an enhanced capability of capturing wind speed variation at small distances, but its resolution still appear to be too coarse to differentiate sufficiently between each turbine.
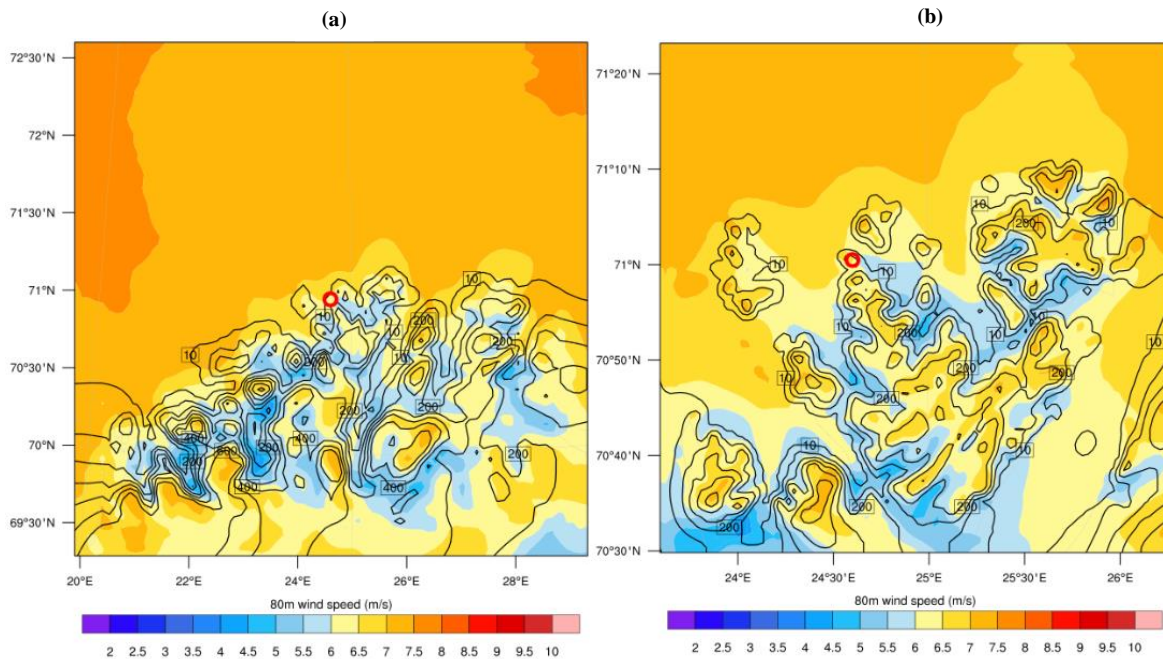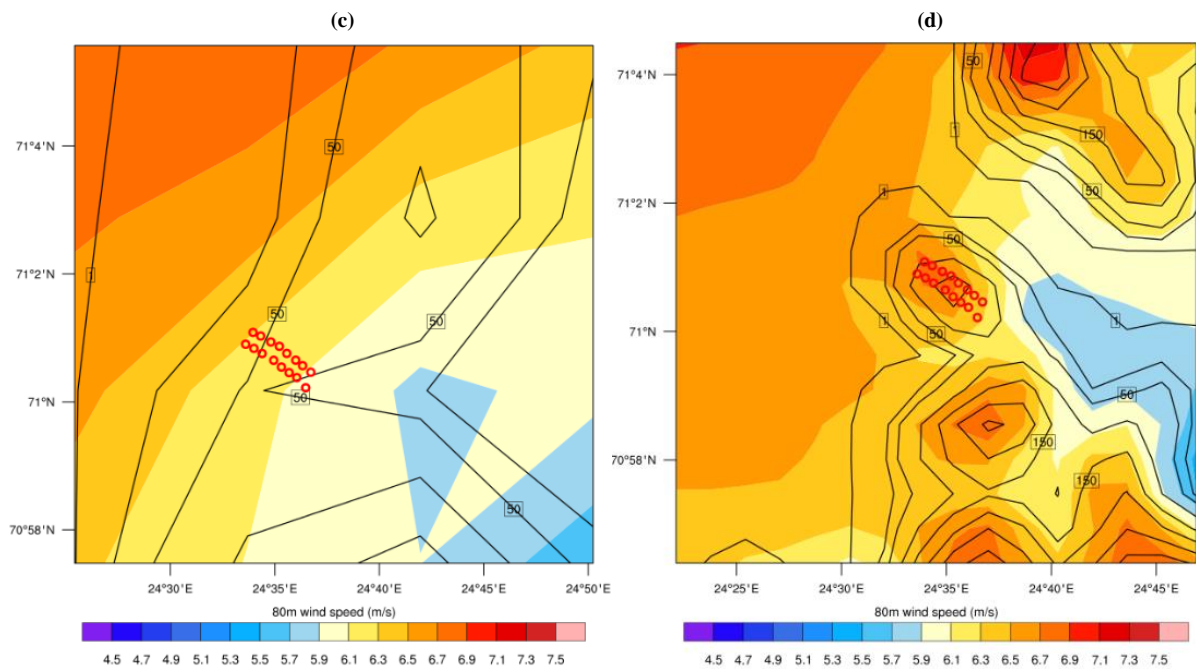
Figure 4.7: (a)-(b) Annual mean wind speed map for D03 and D02, respectively. The estimated wind speed at each indices are constructed by a contour plot. The location of the site is mark with a hollow red circle. (c)-(d) Zoomed versions of (a) and (b), where the small wind speed differences between turbines are made more apparent. The location of each turbine is marked with hollow red circles. Surrounding topography is illustrated by black contour lines for all maps.

The annual distribution of wind speed measured at hub height along with the corresponding D03 WRF wind speed estimation for each turbine in 2017 is displayed conjointly as normalized histograms in Figure 4.1 (a)-(p). Both histograms are semi-transparent in order to illustrate where the wind speed distributions overlay and deviate from each other.

In concordance with previous evaluations, the figure illustrate the WRF model's proneness to overestimate low wind speeds, and underestimate high wind speeds. The highest correlation between the on-site distribution and the WRF model distribution seem to take place at turbines located centrally on the site. These turbines have also shown to measure lower annual mean wind speed, which agrees with previous assumptions that the WRF model estimate lower wind speeds more accurately than higher wind speeds.

As mentioned in section 4.1, bimodal distribution is most apparent for turbines situated in the northwest, and that the second peak tend to plateau towards the southeast of the site, before eventually appearing unimodal. This may suggest the second peak is affected by terrain which increases towards the northeast, implying an shoreward origin for the wind.

55

Although the WRF model appear to capture the bimodal distribution, a tendency among the turbines is evident regarding the overestimation of wind speed for the second peak. As the second peak is assumed particularly terrain dependent, this suggests an underestimation of terrain effect for the D03 WRF model, resulting in higher wind speeds arriving from the shore.
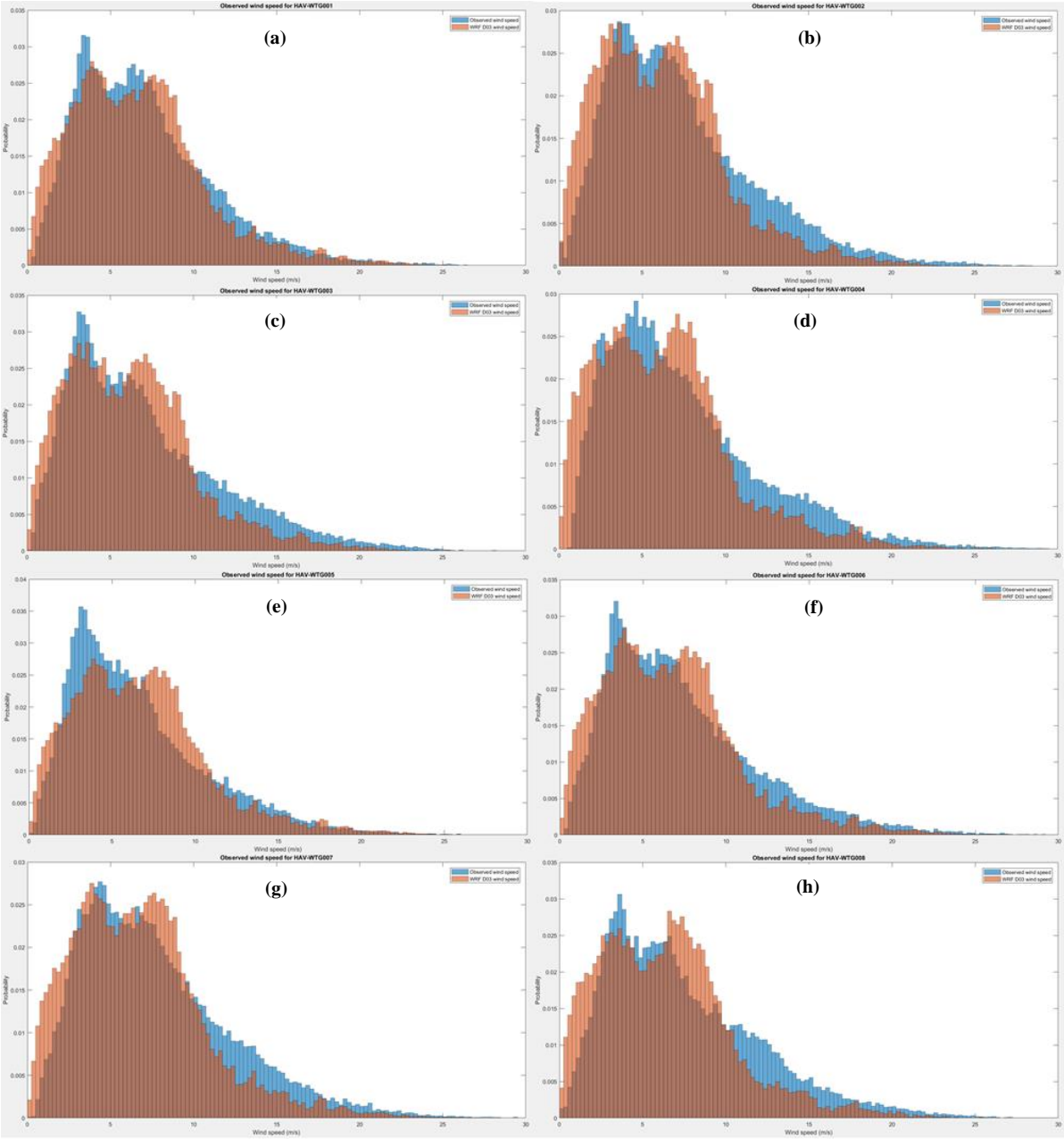
Figure 4.8: (a)-(p) Normalized histograms showing the wind speed distribution for D03 WRF estimate and On-site measurements through 2017 for each wind turbine, respectively.
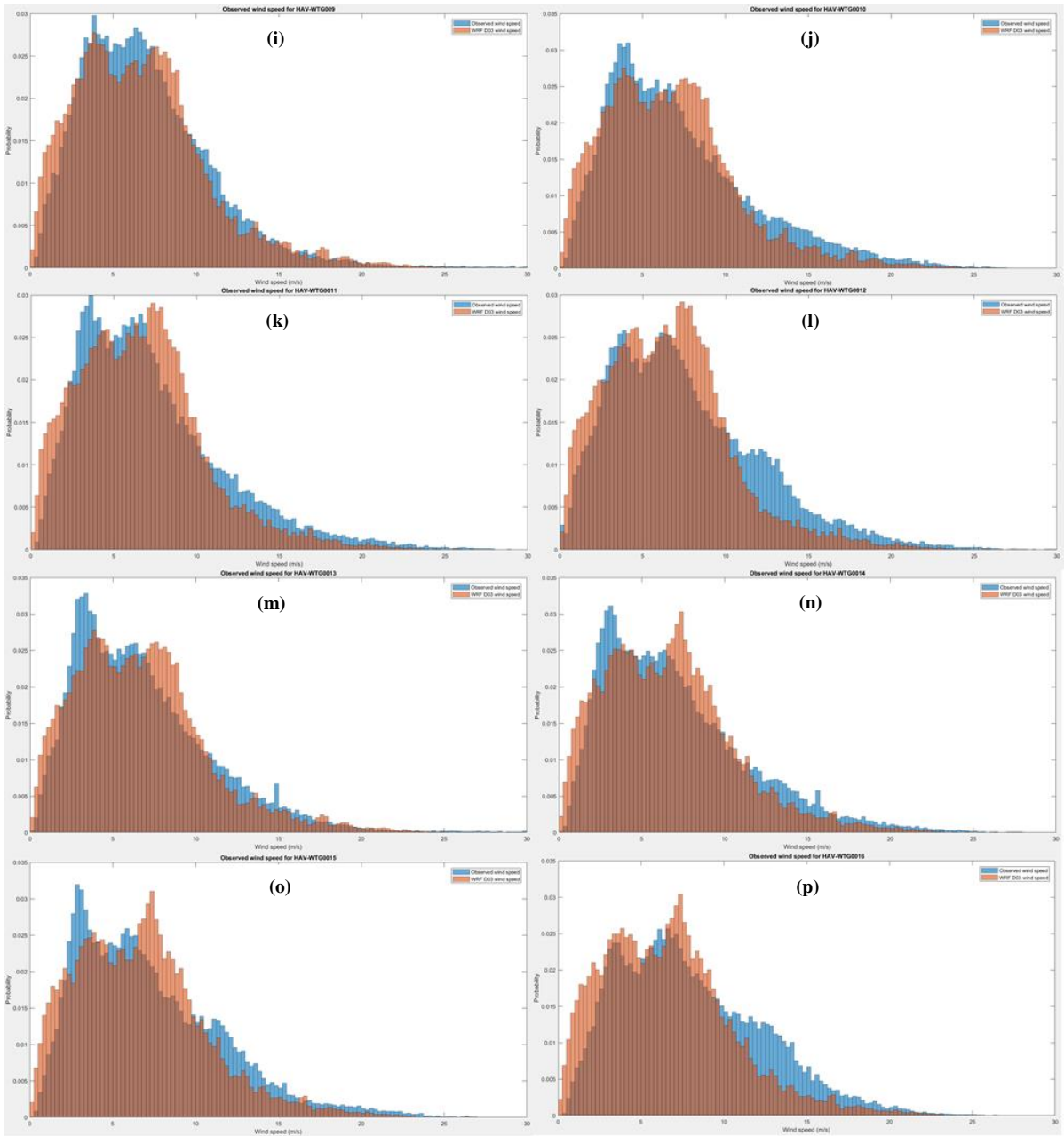
4.2.2 Wind direction analysis

The annual wind direction estimated by the WRF model in 2017 for D02 and D03 is presented in wind roses in Figure 4.9 (a)-(p), at the location of each wind turbine at the site, respectively in pairs. Note that concentric circles representing the frequency of occurrence are set dynamically for each wind rose, and represent the number of wind samples blowing from a particular direction. The entire simulated year compose of 52416 samples in total.

D02 estimates a prevailing wind direction in S and SSW for all turbines, consisting mostly of low speed winds. This may be a result of D02's coarser resolution, causing a more smoothened topography, which allows air to flow more easily over the roughest terrain surrounding the site. As opposed to D03, the prevailing wind direction estimated by D02 does not skew in reference to placement of each turbine. This can be explained by the positioning of the turbines relative to the D02 resolution grid. If the turbines are located at indices enclosed by the same grid points, the bilinear interpolation will produce almost identical results for all turbines.

For D03, the prevailing wind varies for each turbine. For the turbines located furthest east, the prevailing wind originate in the SW, while as we move towards the west side of the site, the estimate indicate a prevailing wind pivoting towards S. This indicates a directional stability for the model domain. Furthermore, the turbines located furthest east of the site experience higher occurrence of wind originating shoreward around SE and ESE.

Both domains estimate the highest wind speed originating in WSW, but also wind coming from WNW-NW holds high speeds for both domains. Wind originating from the ocean is distributed very similarly for both D03 and D02. As the terrain's effect on wind diminishes along this direction, the varying level of terrain smoothening can be neglected, leading to similar results for both domains. Wind originating in the range ENE-ESE mostly compose of moderate wind speeds, and is distributed quite equal by both domains.

59
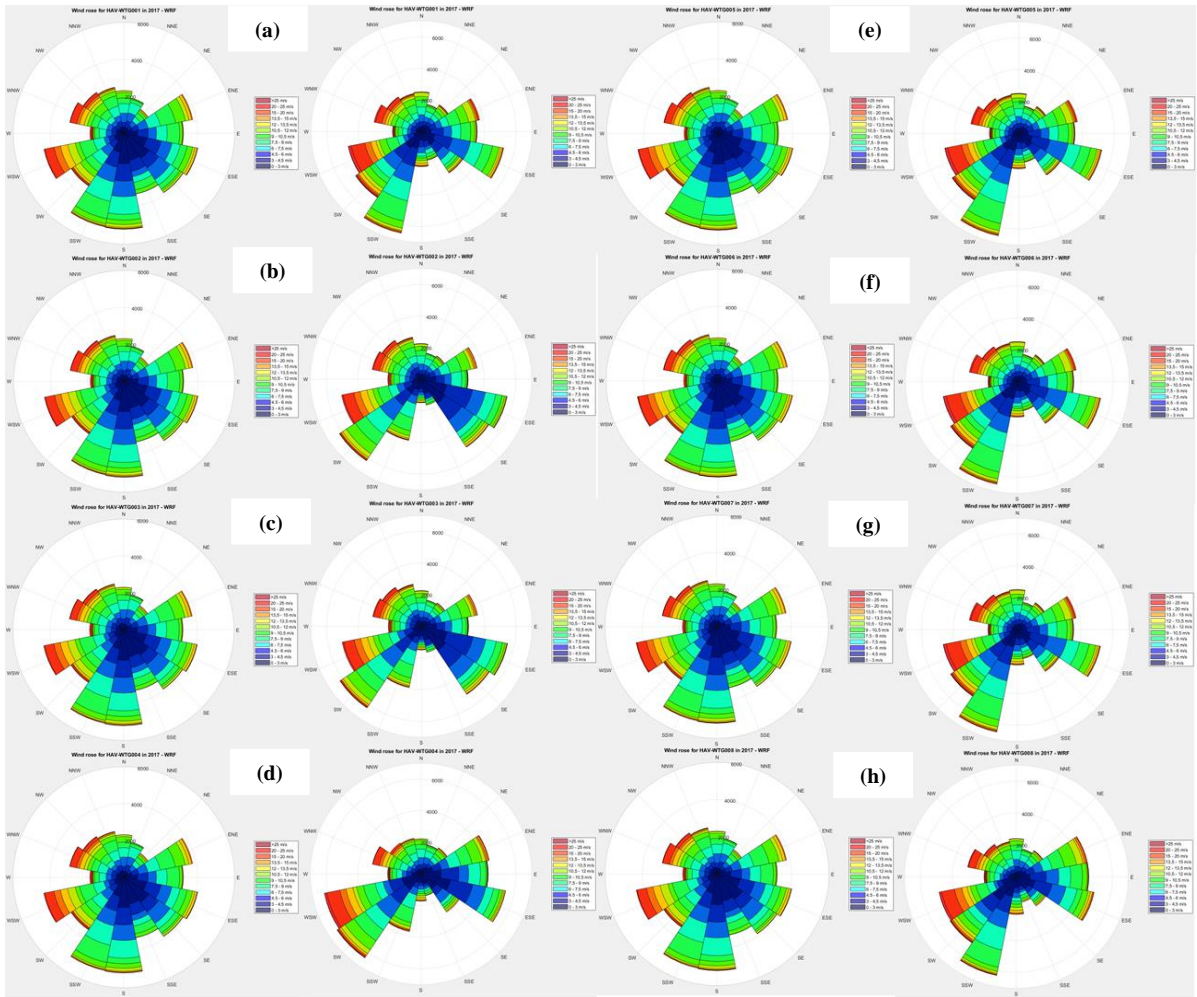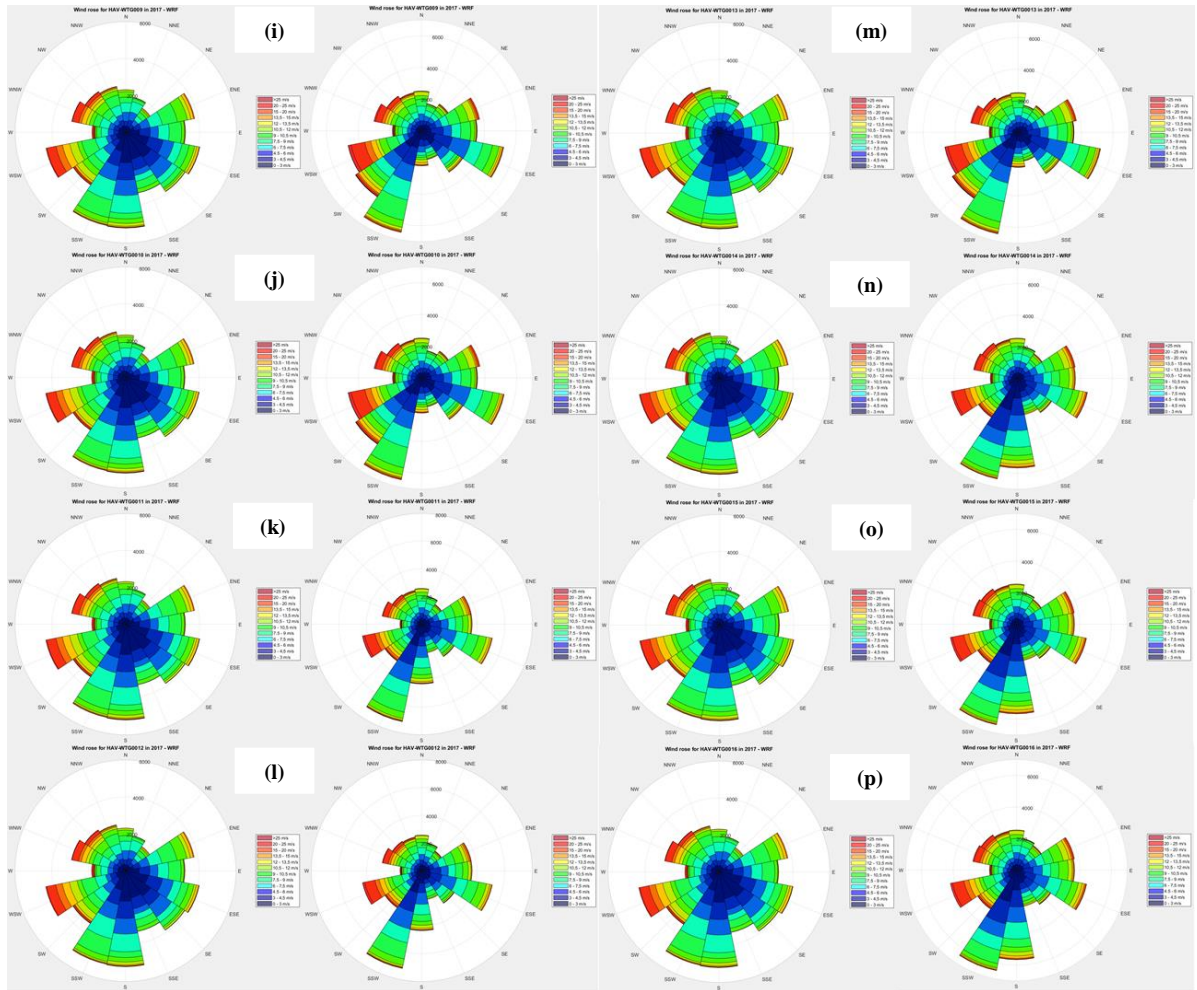
Figure 4.9: (a)-(p) The annual wind direction estimated by the WRF model for D02 and D03 presented in wind roses, at the location of each wind turbine at the site, respectively in pairs.

To get a closer look at how the wind moves in relation to the terrain of each domain, wind vector maps will be used to describe both wind speed and wind direction over the domain topography. In addition to the two innermost WRF domains, D01 will also be included to get a broader view of the wind behaviour, and to illustrate the terrain effect on the surrounding wind for an even lower resolution.

Figure 4.10 (a)-(f) demonstrate the wind field at specific moments in time estimated by each domain of the WRF model used in this thesis. The two moments of interest are chosen for the reason that the WRF model estimated particularly high wind speeds at these points in time. The momentary wind direction at a grid point is allocated by wind vectors. Both the colour and length of the vectors correspond to a specific wind speed, assigned by a vertical colour palette and a reference vector in the southeast corner, respectively. Furthermore, the vectors overlay a topographic contour plot denoted by a horizontal colour palette.

The higher resolution of D03 improves the capturing of peaks in the topography, compared to the coarser domains. As a result, D03 estimates higher wind speed at these peaks, and the resulting steepness surrounding the peaks leads to lower wind speed in the wake. Due to the improved topography interpolation of D03, the wind also curls in a accordance to the terrain to a greater degree than the coarser domains. This may explain the variable directional stability detected from the respective wind roses of D03 and D02.

The directional origin of the wind arriving at the site confirms that wind approximately coming from the southwest has the highest wind speeds. By inspecting Figure 4.10 (f), the reason for the high wind is a low-pressure system north of the site blowing counter clockwise, such that high speed wind arrives at the site with minimum terrain effects. The same weather phenomena is likely to be the reason for the high wind speed in Figure 4.10 (e), although D01 does not capture it.

D01, 12.02.17, 10:30

D01, 26.03.17, 05:50

(e)

(f)

Terrain surrounding Havoygavlen (m)
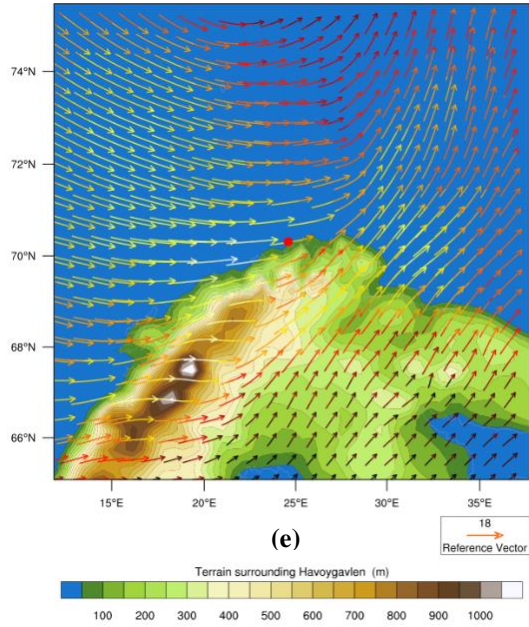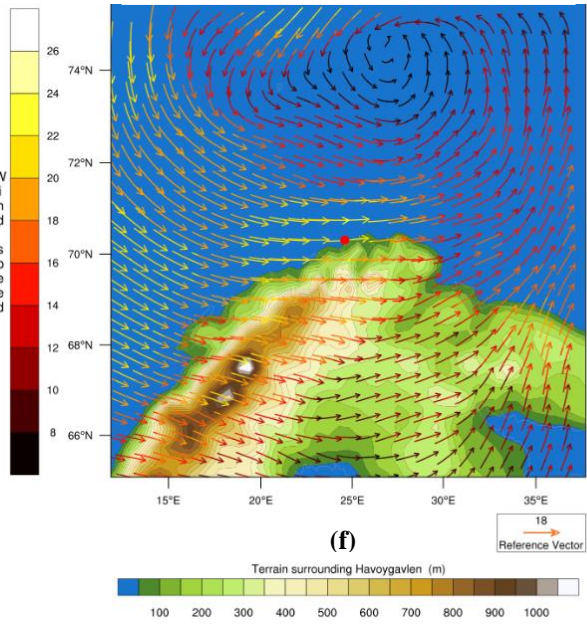
D02, 12.02.17, 10:30

D02, 26.03.17, 05:50

(c)

(d)

Terrain surrounding Havoygavlen (m)

62
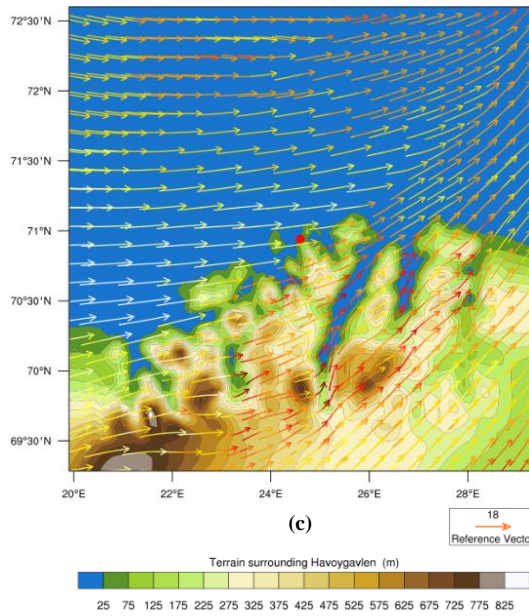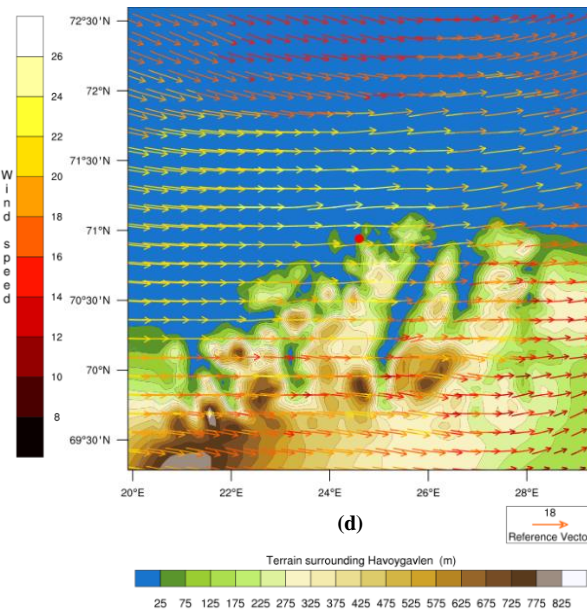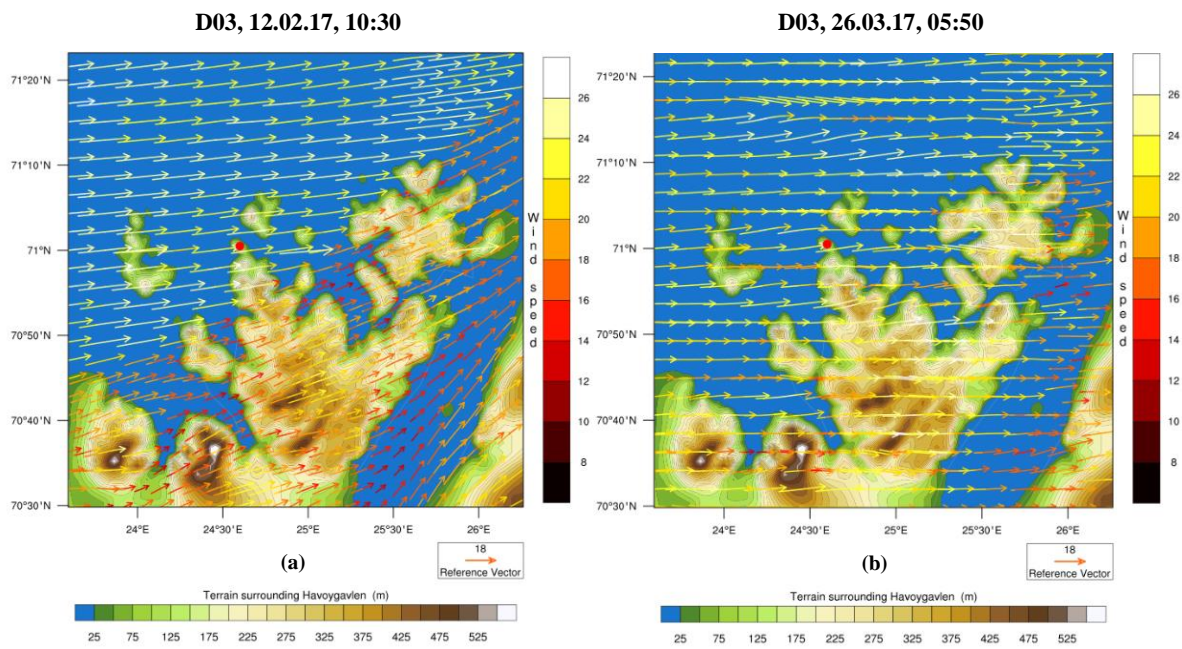
Figure 4.10: (a)-(f) Wind vector maps at two specific moments in time with high wind estimates for each domain of the WRF model used in this thesis, respectively. The momentary wind direction and wind speed at a grid point is allocated by wind vectors, and overlay a topographic contour plot. Note that the topographic colour scale change dynamically, while the wind speed scaling is constant.

Conclusion

In this thesis a wind resource assessment has been carried out for Havøygavlen wind park using the weather research and forecasting model (WRF), with regard to wind speed and wind direction. The WRF model was run for the whole year of 2017 at points of interest, corresponding each turbine on the site at hub height, where on-site measurements were made and compared to the WRF estimates.

RMSE, correlation coefficient and bias indicates limitations of the model regarding accurate forecasting of the site's wind field. Higher simulation resolution showed no apparent reproduction improvements. D03 gave the lowest bias, while D02 provided a lower RMSE and correlation to the on-site measurements. The same predictive tendency was found regarding wind direction. While exclusively examining the Siemens turbine situated on the site, D02 showed the most accurate directional wind forecast. Investigation of the model performance with respect to seasonal variations indicated higher forecasting accuracy for seasons of lower wind speeds. The model exhibited a deficient ability to adjust to sudden changes in wind speed, which often occurred in periods of high wind speeds.

The resolution of the WRF domains failed to capture the high complexity of the surrounding terrain, ultimately leading to an underestimation of the annual wind resources of the site. However, improved accuracy was found when using finer simulation resolution. The same conclusion is illustrated when comparing annual mean wind speed maps for D02 and D03. The maps demonstrate how the finer resolution to a greater extent captures the varying wind resource at each turbine established by the on-site measurements. Additionally, topographic contour lines illustrated how the model resolution smoothens the plateau where the turbines are situated. Consequently, the altitude of the point of interest are underestimated, which may explain why the WRF model accordingly underestimates the annual wind resource of the site.

Wind roses were used to display annual wind direction distribution for both D02 and D03. Both domains estimate the highest wind speed originating in WSW, and generally high wind speeds originating oceanward due to a low terrain effect in these directions. The coarse resolution of D02 induced very small directional variations among the turbines, while D03 displayed greater directional stability leading to differing prevailing wind directions

compared to D02. Wind fields at specific times of high wind speed occurrence for all model domains illustrated how the degree of terrain smoothening affected both the course and the speed of the wind. The enhanced ability to capture the wind's terrain deflection, performed by D03, leads to believe that the higher resolution produces more agreeable wind direction distributions with respect to the actual wind field of the site.

To summarize, the WRF model showed little agreement in regard to forecasting the on-site wind speed measurements, and finer resolution showed no apparent improvement. The model performed more adequate at estimating the annual wind resource of the site, in which a heightened resolution enhanced the predictive performance. The result from the model setup used in this assessment provide valuable knowledge and insight of the site's wind resources, which is transferable to locations of similar climate and terrain. However, the model fails to capture the complexity of the terrain, and underestimates the wind resources to such a degree, it may suggest that other factors have affected the performance of the model. These factors may be an unsuitable model parameterization setup used for this specific case, or due to inadequate input data from ERA-Interim. Before these factors have been studied and tested to further improve the accuracy of the model for the case at hand, it performs insufficiently as an independent wind resource assessment tool at this point.

Further research

Several improvement aspects of the WRF model setup used in this thesis could be further investigated. It is well established that numerical weather models have higher errors in terrain of high complexity. Hence, a sensitive analysis of the correlation trend between simulation resolution and the wind resource assessment accuracy could provide valuable information regarding a potentially ideal resolution for capturing the ruggedness of the terrain, and at what point the trend turns.

The complexity of arctic regions such as the Havøygavlen site introduce challenges to numerical models. It would for that reason be interesting to perform sensitive studies of numerous physical options available to the WRF model. The purpose would be to investigate

what physical options presented in section 3.2.6 that captures the physical properties of Havøygavlen most accurately. If the various options performed distinctly for different seasons, a possible alternative would be to modify the physical options through a whole year according to the performance variations. This would be possible due to the segmentation of the simulation period used in this thesis.

By increasing the number of vertical levels in the domain, as well as distributing the levels manually to improve the ability of adjusting to small-scale changes in topography could possibly enhance the accuracy of the model.

Due to the coarseness of the ERA-Interim data used in this thesis, implementing finer spatial input data similar to the on-site measurements used in this thesis could accompany the ERA-Interim data, which could ultimately improve the accuracy of the input data to the WRF model.

Lastly, it would be interesting to investigate how the model's vertical wind profile is affected by the ruggedness of the nearby terrain. By exploring different locations with the same WRF setup, a correlation between vertical wind profile and topographic ruggedness index (TRI) [37] can be found, which can provide knowledge for the investigation of new potential sites where the TRI is known.

Appendices

Appendix A: Geographic coordinates of the wind turbines at Havøygavlen

Wind turbines	Latitude	Longitude
HAV-WTG001	71.01095	24.600052
HAV-WTG002	71.00951	24.605536
HAV-WTG003	71.007798	24.6121
HAV-WTG004	71.003761	24.608
HAV-WTG005	71.010915	24.582402
HAV-WTG006	71.009153	24.588599
HAV-WTG007	71.007691	24.594766
HAV-WTG008	71.006407	24.600891
HAV-WTG009	71.01271	24.592858
HAV-WTG010	71.015691	24.580131
HAV-WTG011	71.01723	24.572046
HAV-WTG012	71.018187	24.56587
HAV-WTG013	71.014554	24.58694
HAV-WTG014	71.012686	24.573184
HAV-WTG015	71.014022	24.566608
HAV-WTG016	71.01509	24.559993

Appendix B: Namelists used in WRF simulation

Namelist.wps:

```
&share
 wrf_core = 'ARW',
 max_dom = 3,
 start_date = '2017-01-14_00:00:00', '2017-01-14_00:00:00', '2017-01-14_00:00:00', '2017-01-14_00:00:00',
 end_date = '2017-01-22_00:00:00', '2017-01-22_00:00:00', '2017-01-22_00:00:00', '2017-01-22_00:00:00',
 interval_seconds = 21600
 io_form_geogrid = 2,
/

&geogrid
 parent_id         =    1,    1,    2,
 parent_grid_ratio =    1,    5,    5,
 i_parent_start    =    1,   18,   31,
 j_parent_start    =    1,   18,   27,
 e_we              =   50,   76,  101,
 e_sn              =   50,   76,  101,
 geog_data_res = 'default','default','default',
 dx = 25000,
 dy = 25000,
 map_proj = 'polar',
 ref_lat   =   71.012,
 ref_lon   =   24.589,
 truelat1  =   71.012,
 truelat2  =   71.012,
 stand_lon =   24.589,


 geog_data_path = '/global/work/EnerCli/geog/'
/

&ungrib
 out_format = 'WPS',
 prefix = 'FILE',
/

&metgrid
 fg_name = 'FILE'
 io_form_metgrid = 2,
/
```

Namelist.input:

```
&time_control
 run_days                        = 8,
 run_hours                       = 0,
 run_minutes                     = 0,
 run_seconds                     = 0,
start_year = 2017, 2017, 2017, 2017 ,
start_month = 01, 01 , 01 , 01 ,
start_day = 14,14,14, 14,
 start_hour                      = 00,    00,    00,
 start_minute                    = 00,    00,    00,
 start_second                    = 00,    00,    00,
end_year = 2017, 2017, 2017, 2017,
end_month = 01, 01, 01, 01,
end_day = 22, 22, 22, 22,
 end_hour                        = 00,    00,    00,
 end_minute                      = 00,    00,    00,
 end_second                      = 00,    00,    00,
 interval_seconds                = 21600
 input_from_file                 = .true.,.true.,.true.,
 history_interval                = 10,    10,    10,
 frames_per_outfile              = 100000, 100000, 100000,
 restart                         = .false.,
 restart_interval                = 50000,
 io_form_history                 = 2
 io_form_restart                 = 2
 io_form_input                   = 2
 io_form_boundary                = 2
 debug_level                     = 0
/


&domains
time_step                        = 150,
time_step_fract_num              = 0,
time_step_fract_den              = 1,
max_dom                          = 3,
e_we                             = 50,     76,    101,
e_sn                             = 50,     76,    101,
e_vert                           = 40,    40,    40,
p_top_requested                  = 5000,
num_metgrid_levels               = 38,
num_metgrid_soil_levels          = 4,
dx                               = 25000, 5000,  1000,
dy                               = 25000, 5000,  1000,
grid_id                          = 1,     2,     3,
parent_id                        = 1,     1,     2,
i_parent_start                   = 1,     18,    31,
j_parent_start                   = 1,     18,    27,
parent_grid_ratio                = 1,     5,     5,
parent_time_step_ratio           = 1,     5,     5,
feedback                         = 1,
smooth_option                    = 0
/
```

```
&physics
physics_suite                    = 'CONUS'
radt                             = 30,     30,      30,
bldt                             = 0,      0,       0,
num_soil_layers                  = 4,
num_land_cat                     = 21,
sf_urban_physics                 = 0,      0,       0,
surface_input_source             = 1,
/

&fdda
/


&dynamics
diff_opt                         = 1,       1,       1,
km_opt                           = 4,       4,       4,
diff_6th_opt                     = 0,       0,       0,
diff_6th_factor                  = 0.12,    0.12,    0.12,
base_temp                        = 290.
damp_opt                         = 0,
zdamp                            = 5000.,   5000.,   5000.,
dampcoef                         = 0.2,     0.2,     0.2
khdif                            = 0,       0,       0,
kvdif                            = 0,       0,       0,
non_hydrostatic                  = .true., .true., .true.,
moist_adv_opt                    = 1,       1,       1,
scalar_adv_opt                   = 1,       1,       1,
gwd_opt                          = 0,
epssm                            = 0.1,    0.1,     0.1,
w_damping                        = 0
time_step_sound                  = 4,       4,       4,
/

&bdy_control
spec_bdy_width                   = 5,
spec_zone                        = 1,
relax_zone                       = 4,
specified                        = .true., .false.,.false.,
nested                           = .false., .true., .true.,
/

&grib2
/

&namelist_quilt
nio_tasks_per_group = 0,
nio_groups = 1,
/
```

Appendix D: Script showing data extraction at points of interest:

```
begin

in      = addfile(filename,"r")

Times = wrf_user_getvar(in,"times",-1) ; gets "times variable" for entire simulation period
ntimes=dimsizes(Times)      ; number of times in the fil
times=ispan(0,ntimes-1,1);


;*************************************************
;  - Select lon & lat of the point of interest -
;*************************************************
; - The function wrf_user_ll_to_ij find the nearest grid point for a specific lat and lon


Position=new((/2,16/),double,0)
Position(0,0) = 24.600052     ; HAV-WTG001 longitude
Position(1,0) = 71.01095      ; HAV-WTG001 Latitude
Position(0,1) = 24.605536     ; HAV-WTG002 Longitude
Position(1,1) = 71.00951      ; HAV-WTG002 Latitude
Position(0,2) = 24.6121       ; HAV-WTG003 Longitude
Position(1,2) = 71.007798     ; HAV-WTG003 Latitude
Position(0,3) = 24.608        ; HAV-WTG004 Longitude
Position(1,3) = 71.003761     ; HAV-WTG004 Latitude
Position(0,4) = 24.582402     ; HAV-WTG005 Longitude
Position(1,4) = 71.010915     ; HAV-WTG005 Latitude
Position(0,5) = 24.588599     ; HAV-WTG006 Longitude
Position(1,5) = 71.009153     ; HAV-WTG006 Latitude
Position(0,6) = 24.594766     ; HAV-WTG007 Longitude
Position(1,6) = 71.007691     ; HAV-WTG007 Latitude
Position(0,7) = 24.600891     ; HAV-WTG008 Longitude
Position(1,7) = 71.006407     ; HAV-WTG008 Latitude
Position(0,8) = 24.592858     ; HAV-WTG009 Longitude
Position(1,8) = 71.012710     ; HAV-WTG009 Latitude
Position(0,9) = 24.580131     ; HAV-WTG010 Longitude
Position(1,9) = 71.015691     ; HAV-WTG010 Latitude
Position(0,10) = 24.572046    ; HAV-WTG011 Longitude
Position(1,10) = 71.01723     ; HAV-WTG011 Latitude
Position(0,11) = 24.56587     ; HAV-WTG012 Longitude
Position(1,11) = 71.018187    ; HAV-WTG012 Latitude
Position(0,12) = 24.58694     ; HAV-WTG013 Longitude
Position(1,12) = 71.014554    ; HAV-WTG013 Latitude
Position(0,13) = 24.573184    ; HAV-WTG014 Longitude
Position(1,13) = 71.012686    ; HAV-WTG014 Latitude
Position(0,14) = 24.566608    ; HAV-WTG015 Longitude
Position(1,14) = 71.014022    ; HAV-WTG015 Latitude
Position(0,15) = 24.559993    ; HAV-WTG016 Longitude
Position(1,15) = 71.01509     ; HAV-WTG016 Latitude
```

```
; Convert position to index in WRF
res = True
res@returnInt = True            ; Note: Integer points
Point=wrf_user_ll_to_ij(in,Position(0,:),Position(1,:),res);
Point=Point-1                   ; Convert to NCL subscript

res@returnInt = False           ; NOTE: exact points
XPoint=wrf_user_ll_to_ij(in,Position(0,:),Position(1,:),res);
XPoint=XPoint-1                 ; Convert to NCL subscript

XLON = in->XLONG(0,:,:);
XLAT = in->XLAT(0,:,:);
U80 = new((/ntimes,16/),float,0)
V80 = new((/ntimes,16/),float,0)
W80 = new((/ntimes,16/),float,0)
xU80 = U80
xV80 = V80
xW80 = W80
mxU80 = U80
mxV80 = V80

; Wind and Height
u = wrf_user_getvar(in,"ua",times)        ; u averaged to mass points
v = wrf_user_getvar(in,"va",times)        ; v averaged to mass points
w = wrf_user_getvar(in,"wa",times)        ; w averaged to mass points

height  = wrf_user_getvar(in, "z",0)  ; height is the vertical coordinate
ter = wrf_user_getvar(in, "ter",0)    ; model terrain height

; Conform data to Terrain Height
nheight = conform(height,ter,(/1,2/)) ; assuming height is a 3d array and ter is a 2d array
height = height - nheight

;*************************************************************
; Interpolate wind speed and wind direction at 80m height  *
;*************************************************************


; Interpolate U,V to 80 Meters
cheight=conform_dims(dimsizes(u),height,(/1,2,3/))
u_plane = wrf_user_intrp3d(u,cheight,"h", 80,0.,False)
v_plane = wrf_user_intrp3d(v,cheight,"h", 80,0.,False)
w_plane = wrf_user_intrp3d(w,cheight,"h", 80,0.,False)

do p=0,15
   U80(times,p)=u_plane(times,Point(1,p),Point(0,p));
   V80(times,p)=v_plane(times,Point(1,p),Point(0,p));
   W80(times,p)=w_plane(times,Point(1,p),Point(0,p));
end do

; Interpolation to exact location
ilon=ispan(0,99,1);
ilat=ilon;
do p=0,15
   xU80(times,p)=linint2_points(ilon,ilat,u_plane,0,XPoint(0,p),XPoint(1,p),0)
   xV80(times,p)=linint2_points(ilon,ilat,v_plane,0,XPoint(0,p),XPoint(1,p),0)
   xW80(times,p)=linint2_points(ilon,ilat,w_plane,0,XPoint(0,p),XPoint(1,p),0)
end do
```

Appendix C: Script showing interpolation between all simulation segments:

```
for n = 1:nfiles

% For each segment extract u and v components at points of interest
UU80{n} = xU80;

VV80{n} = xV80;

end

H12     = 12*6;      %12 hours times 6 10-min values.
Week    = 7*24*6;    %1 week has 7*24*6 = 1008 10-min values
D       = 24*6;      % 1 day has 24*6 = 144 10-min values


for n = 1:length(files(:,1))-1
disp(n)
FY_M0000 = 1+1008*(n-1);
FY_S1150 = 1008*n-H12;
FY_S1200 = FY_S1150 +1;
FY_S2350 = 1008*n;

W_M0000  = D+1;
W_S1150  = D+1008-H12;
W_S1200  = W_S1150 +1;
W_S2350  = 1153-1;

% Week n
Time(FY_M0000:FY_S1150,1) = T{n}(W_M0000:W_S1150);

U80(:,FY_M0000:FY_S1150) = UU80{n}(:,W_M0000:W_S1150);

V80(:,FY_M0000:FY_S1150) = VV80{n}(:,W_M0000:W_S1150);

% temp week n
Time(FY_S1200:FY_S2350,1) = T{n}(W_S1200:W_S2350);

U80temp1 = UU80{n}(:,W_S1200:W_S2350);

V80temp1 = VV80{n}(:,W_S1200:W_S2350);


%temp week n+1
dt(FY_S1200:FY_S2350,1) = T{n+1}(H12+1:D);

U80temp2 = UU80{n+1}(:,H12+1:D);

V80temp2 = VV80{n+1}(:,H12+1:D);

%Interpolate the 12 last hours saturday
d = H12;
x = linspace(0,1,d);
```

```
U80(1,FY_S1200:FY_S2350)  = (U80temp1(1,:).*(1-x)+U80temp2(1,:).*x);
U80(2,FY_S1200:FY_S2350)  = (U80temp1(2,:).*(1-x)+U80temp2(2,:).*x);
U80(3,FY_S1200:FY_S2350)  = (U80temp1(3,:).*(1-x)+U80temp2(3,:).*x);
U80(4,FY_S1200:FY_S2350)  = (U80temp1(4,:).*(1-x)+U80temp2(4,:).*x);
U80(5,FY_S1200:FY_S2350)  = (U80temp1(5,:).*(1-x)+U80temp2(5,:).*x);
U80(6,FY_S1200:FY_S2350)  = (U80temp1(6,:).*(1-x)+U80temp2(6,:).*x);
U80(7,FY_S1200:FY_S2350)  = (U80temp1(7,:).*(1-x)+U80temp2(7,:).*x);
U80(8,FY_S1200:FY_S2350)  = (U80temp1(8,:).*(1-x)+U80temp2(8,:).*x);
U80(9,FY_S1200:FY_S2350)  = (U80temp1(9,:).*(1-x)+U80temp2(9,:).*x);
U80(10,FY_S1200:FY_S2350) = (U80temp1(10,:).*(1-x)+U80temp2(10,:).*x);
U80(11,FY_S1200:FY_S2350) = (U80temp1(11,:).*(1-x)+U80temp2(11,:).*x);
U80(12,FY_S1200:FY_S2350) = (U80temp1(12,:).*(1-x)+U80temp2(12,:).*x);
U80(13,FY_S1200:FY_S2350) = (U80temp1(13,:).*(1-x)+U80temp2(13,:).*x);
U80(14,FY_S1200:FY_S2350) = (U80temp1(14,:).*(1-x)+U80temp2(14,:).*x);
U80(15,FY_S1200:FY_S2350) = (U80temp1(15,:).*(1-x)+U80temp2(15,:).*x);
U80(16,FY_S1200:FY_S2350) = (U80temp1(16,:).*(1-x)+U80temp2(16,:).*x);

V80(1,FY_S1200:FY_S2350)  = (V80temp1(1,:).*(1-x)+V80temp2(1,:).*x);
V80(2,FY_S1200:FY_S2350)  = (V80temp1(2,:).*(1-x)+V80temp2(2,:).*x);
V80(3,FY_S1200:FY_S2350)  = (V80temp1(3,:).*(1-x)+V80temp2(3,:).*x);
V80(4,FY_S1200:FY_S2350)  = (V80temp1(4,:).*(1-x)+V80temp2(4,:).*x);
V80(5,FY_S1200:FY_S2350)  = (V80temp1(5,:).*(1-x)+V80temp2(5,:).*x);
V80(6,FY_S1200:FY_S2350)  = (V80temp1(6,:).*(1-x)+V80temp2(6,:).*x);
V80(7,FY_S1200:FY_S2350)  = (V80temp1(7,:).*(1-x)+V80temp2(7,:).*x);
V80(8,FY_S1200:FY_S2350)  = (V80temp1(8,:).*(1-x)+V80temp2(8,:).*x);
V80(9,FY_S1200:FY_S2350)  = (V80temp1(9,:).*(1-x)+V80temp2(9,:).*x);
V80(10,FY_S1200:FY_S2350) = (V80temp1(10,:).*(1-x)+V80temp2(10,:).*x);
V80(11,FY_S1200:FY_S2350) = (V80temp1(11,:).*(1-x)+V80temp2(11,:).*x);
V80(12,FY_S1200:FY_S2350) = (V80temp1(12,:).*(1-x)+V80temp2(12,:).*x);
V80(13,FY_S1200:FY_S2350) = (V80temp1(13,:).*(1-x)+V80temp2(13,:).*x);
V80(14,FY_S1200:FY_S2350) = (V80temp1(14,:).*(1-x)+V80temp2(14,:).*x);
V80(15,FY_S1200:FY_S2350) = (V80temp1(15,:).*(1-x)+V80temp2(15,:).*x);
V80(16,FY_S1200:FY_S2350) = (V80temp1(16,:).*(1-x)+V80temp2(16,:).*x);


end

% Add week 52 from monday 00:00 to sunday 23.50
n = length(files(:,1));
FY_M0000 = 1+1008*(n-1);
FY_S1150 = 1008*n-H12;
FY_S1200 = FY_S1150 +1;
FY_S2350 = 1008*n;

W_M0000  = D+1;
W_S1150  = D+1008-H12;
W_S1200  = W_S1150 +1;
W_S2350  = 1153-1;



% Week n
Time(FY_M0000:FY_S2350,1)    = T{n}(W_M0000:W_S2350);

U80(:,FY_M0000:FY_S2350)     = UU80{n}(:,W_M0000:W_S2350);

V80(:,FY_M0000:FY_S2350)     = VV80{n}(:,W_M0000:W_S2350);

% The resulting matrixes have 16 rows corresponding to each wind turbine at Havøygavlen.
% Below is an example of extracting the wind components at HAV-WTG001:

u80     = U80(1,:);

v80     = V80(1,:);

w80     = W80(1,:);
```

Appendix E: Script showing how to plot annual mean wind speed map:

```
begin

type = "png"

 wks = gsn_open_wks(type,"WindSpeed_Terrain_plot")

; "fils" include all 52 wrfout-files, while "Zin" is one spesific wrfout-file
;  due to the variable being extracted is time-independent
time = 1
ntimes = 52

 Zin  = addfile(filename,"r")

 f    = addfiles (fils, "r")
 ListSetType (f, "cat")         ; concatenate f

 height  = wrf_user_getvar(Zin, "z",time)  ; height is the vertical coordinate
 ter = wrf_user_getvar(Zin, "ter",time)    ; model terrain height

; Conform data to Terrain Height
 nheight = conform(height,ter,(/1,2/)) ; assuming height is a 3d array and ter is a 2d array
 height = height - nheight


do i=0,ntimes-1

 U    = f[i]->U(144::,:,:,:)  ; read U but cut first day
 V    = f[i]->V(144::,:,:,:)  ; read V but cut first day

; Unstagger U and V components to obtain variables average to mass point
 ua = wrf_user_unstagger(U,U@stagger)
 va = wrf_user_unstagger(V,V@stagger)

; Interpolate ua and va to 80 meters
cheight=conform_dims(dimsizes(ua),height,(/1,2,3/))
 U_plane = wrf_user_intrp3d(ua,cheight,"h", 80,0.,False)
 V_plane = wrf_user_intrp3d(va,cheight,"h", 80,0.,False)

; caculate wind speed at 80 meters from U and V components
 Wspd = sqrt(U_plane^2+V_plane^2)


; The following procedure shows a portion of how each segment is attached to a previously existing array
; In reality, this was done for all 52 segments
if (i.eq.0) then
 Wspd0 = Wspd
end if

if (i.eq.1) then
 Wspd1 = Wspd
end if

 Wspd := array_append_record (Wspd0,Wspd1,0)


;Averaging wind speed with respect to time dimension
 WS = dim_avg_n( Wspd,0)
```

```
;---Change the metadata in plot
  WS@description = "80m wind speed"
  WS@units       = "m/s"


;---Mean wind speed contour plot

  WS_res                     = True
  WS_res@cnFillOn            = True
  WS_res@ContourParameters   = (/2,10,0.5/)
  WS_res@lbTitleString       = WS@description + " (" + WS@units + ")"

  contour_WS = wrf_contour(Zin,wks,WS,WS_res)


;---Topographic line contour plot


  t_res                          = True
  t_res@cnLineColor              = "Black"
  t_res@cnLevelSelectionMode     = "ExplicitLevels"
  t_res@cnLevels                 = (/10,100,200,300,400,500,600/)
  t_res@cnLineLabelBackgroundColor   = -1    ; transparent
  t_res@cnLineThicknessF         = 2.5
  t_res@cnInfoLabelOn       = False
  t_res@cnInfoLabelOrthogonalPosF = -0.04
  t_res@cnInfoLabelString = "Contour line intervals of 100m"

  contour_ter = wrf_contour(Zin,wks,ter,t_res)

  mapres = True
  mapres@mpOutlineOn = True
  pltres = True
  pltres@PanelPlot = True

; Poly marker for Havøygavlen
  polyres = True
  polyres@gsMarkerIndex = 4
  polyres@gsMarkerSizeF = 13.
  polyres@gsMarkerThicknessF = 8
  polyres@gsMarkerColor  = "red"

;---Overlay plots on map and draw.
map = wrf_map_overlays(Zin,wks,(/contour_WS,contour_ter/),pltres,mapres)


lon = 24.60005      ; Havøygavlen longitude
lat = 71.01095       ; Havøygavlen Latitude


Havoygavlen = gsn_add_polymarker(wks,map,lon,lat,polyres)


draw(map)
   frame(wks)

end
```

5 Bibliography

[1]   IEA, "World energy outlook 2018, executive summary," November 2018. [Online].
      Available: https://webstore.iea.org/download/summary/190?fileName=English-WEO-
      2018-ES.pdf.

[2]   BP, "BP Energy Outlook, 2019 edition, Executive summary," 2019. [Online].
      Available: https://www.bp.com/content/dam/bp/business-
      sites/en/global/corporate/pdfs/energy-economics/energy-outlook/bp-energy-outlook-
      2019.pdf.

[3]   IEA, "Global Energy & CO2 Status Report 2017," [Online]. Available:
      https://www.iea.org/publications/freepublications/publication/GECO2017.pdf.

[4]   Y. Birkelund, S. Alessandrini, Ø. Byrkjedal and L. D. Monache, "Wind power
      prediction in complex terrain using analog ensembles," *Journal of Physics: Conference
      Series,* 10 2018.

[5]   M. Meisingset, T. M. Ohnstad, K. Uhlen and L. R. Strand, "Field tests and modelling
      of a wind farm with doubly fed induction generators," *Wind energy,* pp. 333-344,
      2005.

[6]   K. Solbakken and Y. Birkelund, "Evaluation of the Weather Research and Forecasting
      (WRF) model with respect to wind in complex terrain," *Journal of Physics:
      Conference Series,* 10 2018.

[7]   Ø. Byrkjedal, E. Berge and K. Vindteknikk AS, "The Use of WRF for Wind Resource
      Mapping in Norway," 1 2008.

[8]   D. Snieckus, "Conquering the Arctic," *Recharge,* January 2013.

[9] K. A. Rosvold, "Havøygavlen - vindpark," 26 September 2018. [Online]. Available: https://snl.no/Hav%C3%B8ygavlen_-_vindpark. [Accessed 15 October 2019].

[10] W. C. Skamarock, J. B. Klemp, J. Dudhia, D. O. Gill, D. M. Barker, W. Wang and J. G. Powers, "A Description of the Advanced Research WRF Version 3," 2008.

[11] J. M. McDonough, "Lectures in elementary fluid dynamics," [Online]. Available: http://web.engr.uky.edu/~acfd/me330-lctrs.pdf.

[12] J. Andrews and Nick Jelley, Energy Science, principles, technologies, and impacts, Oxford University Press, 2013.

[13] T. Letcher, Wind Energy Engineering: A Handbook for Onshore and Offshore Wind Turbines, Academic Press, 2017, pp. 17-24.

[14] REUK.co.uk, "Betz Limit," [Online]. Available: http://www.reuk.co.uk/wordpress/wind/betz-limit/.

[15] windpower.org, "The Power Curve of a Wind Turbine," Danish wind industry association, 2000. [Online]. Available: http://ele.aut.ac.ir/~wind/en/tour/wres/pwr.htm.

[16] D. E. Weir, "Vindkraft - Produksjon i 2013," NVE, 2014.

[17] NVE, "Vind- og produksjonsindekser for vindkraft i Norge," 2018.

[18] S. Emeis, Wind Energy Meteorology Atmospheric Physics for Wind, Springer-Verlag Berlin Heidelberg, 2013.

[19] ECMWF, "Era-interim," May 2019. [Online]. Available: https://www.ecmwf.int/en/forecasts/datasets/reanalysis-datasets/era-interim.

[20] D. Dee, S. Uppala, A. Simmons, P. Berrisford, P. Poli, S. Kobayashi, U. Andrae, M. Balmaseda, G. Balsamo, P. Bauer, P. Bechtold and others, "The era-interim reanalysis: Configuration and performance of the data assimilation system," *Quarterly Journal of the Royal Meteorological Society,* pp. 137: 553-597, 2011.

[21] P. Berrisford, D. P. Dee, P. Poli, R. Brugge, M. Fielding, M. Fuentes, P. W. Kållberg, S. Kobayash, S. Uppala and A. Simmons, "The ERA-Interim archive Version 2.0," 2011.

[22] J. Michalakes, S. Chen, J. Dudhia, L. Hart, J. Klemp, J. Middlecof and W. Skamarock, "Development of a next generation regional weather research and forecast model.," *In Developments in Teracomputing: Proceedings ofthe Ninth ECMWF Workshop on the use of high performance computing in meteorology,* no. volume 1, pp. 269-276, 2001.

[23] D. M. Demirtaş, "WRF PreProcessing System (WPS)," Alanya, Turkey, 2011.

[24] J. Dudhia, "WRF Modeling System overview," 2011. [Online]. Available: http://www2.mmm.ucar.edu/wrf/users/tutorial/201901/dudhia_overview.pdf.

[25] D. Gill and M. Pyle, "Nesting in WRF," funnel.sfsu.edu, 2012. [Online]. Available: http://funnel.sfsu.edu/students/luyilin/Lu_Yilin/wrf/WRFNesting-small.pdf.

[26] W. C. Skamarock, J. B. Klemp, J. Dudhia, D. O. Gill, Z. Liu, B. Berner, W. Wang, D. M. Barker, M. G. Duda, J. G. Powers and X.-y. Huang, "A Description of the Advanced Research WRF Version 4," 2019.

[27] W. Wang, C. Bruyère, M. Duda, J. Dudhia, D. Gill, M. Kavulich, K. Werner, M. Chen, L. Hui-Chuan, J. Michalakes, S. Rizvi, X. Zhang, J. Berner, D. Munoz-Esparza, B. Reen, S. Ha and K. Fossell, "WRF ARW Version 4 Modeling System User's Guide," January 2019.

[28] Earth System Research Laboratory NOAA, "Wrf namelist.input file description," [Online]. Available: http://esrl.noaa.gov/gsd/wrfportal/namelist_input_option.html.

[29] M. Diamantakis, "Time stepping schemes for atmospheric modelling: alternatives to SLSI method," 2014. [Online]. Available: https://confluence.ecmwf.int/download/attachments/31917013/Diamantakis_Time-stepping.pdf.

[30] L. J. Wicker and W. C. Skamarock, Time-splitting methods for elastic models using forward time schemes, Monthly weather review, 2002, pp. 130, 2088–2097.

[31] D. R. Durran, Numerical methods for wave equations in geophysical fluid dynamics, volume 32, Springer Science & Business Media, 2013.

[32] Z. Pan, E. S. Takle, W. J. Gutowski and R. Turner, "Long Simulation of Regional Climate as a Sequence of Short Segments," *Monthly Weather Review 127(3),* 1999.

[33] The NCAR Command Language (Version 6.1.2) [Software], 2013. [Online]. Available: http://www.ncl.ucar.edu/.

[34] W. C. Skamarock, J. B. Klemp, J. Dudhia, D. O. Gill, D. M. Barker, W. Wang and J. G. Powers, "Wrf model users' page," April 2016. [Online]. Available: http://www2.mmm.ucar.edu/wrf/users/index.html.

[35] NRCS National water and climate center, "Wind Rose Resources," [Online]. Available: https://www.wcc.nrcs.usda.gov/climate/windrose.html. [Accessed 2019].

[36] S. A. McLeod, "What does a box plot tell you? Simply Psychology.," 19 July 2019. [Online]. Available: https://www.simplypsychology.org/boxplots.html.

[37] S. J. Riley, S. D. DeGloria and R. Elliot, "A terrain ruggedness index that quantifies topographic heterogeneity," *Intermountain Journal of Sciences,* no. vol. 5, No. 1-4, 1999.